In Situ Light Scattering Analysis of the Curing Behavior and the Mechanical Properties of Thermoset Polymers

by
Michael Frederick Aldridge

A dissertation submitted in partial fulfillment
of the requirements for the degree of
Doctor of Philosophy
(Materials Science and Engineering)
in the University of Michigan
2014

Doctoral Committee:

Professor John Kieffer, Chair
Assistant Professor Anish Tuteja
Professor Anthony M. Waas
Professor Alan S. Wineman

TABLE OF CONTENTS

LIST OF FIGURES

LIST OF TABLES

ABSTRACT

Thermoset resins are used in carbon fiber composites because of their superior stiffness and improved thermal resistance over thermoplastics. In the manufacturing of these composites, the resin is infused into a carbon textile, and cured at a proscribed temperature and pressure. The presence of carbon fibers may influence the progress of the cure reaction and the resulting mechanical properties of the resin. Mechanical testing of composite structures reveals that the resulting composite has mechanical properties that diverge from those predicted by assuming bulk mechanical properties of the constituent materials.

This dissertation describes the investigation of how chemistry and thermal history influence the mechanical properties of thermoset polymers. The relationship between mechanical properties and molecular structure is probed using a novel combination of, Brillouin and Raman light scattering techniques. Brillouin scattering yields information about the mechanical and transport properties of a material, while Raman scattering is used to detect changes in the molecular structure of the material. These techniques are used concurrently, *in-situ* during cure, sharing a single optical setup, probing the chemical state and mechanical properties of the same focal volume within the sample.

Using this approach, two archetypical thermoset polymers are studied as a function of the initial chemistry and thermal history: Grubb's catalyzed dicyclopentadiene, and an epoxy resin cured with an amine hardener. Raman

spectra are used to develop kinetic models of the polymer cure behavior. However, the mechanical properties do not map linearly onto the degree of cure, but instead require one to account for relaxation processes that occur during and after cure. Finally, concurrent micro-Raman and -Brillouin scattering are used to resolve the spatial variations of the mechanical properties of the fully cured epoxy matrix in between carbon fibers. The elastic modulus decreases linearly with fiber density in regions of the matrix with closely packed fibers. Comparing Raman and Brillouin data reveals that the observed inhomogeneity of elastic properties is not due to residual stresses, but likely results from structural reorganization of the polymer in the interphase region.

Chapter 1

Background and Motivation

1.1 Motivation and Project Overview

Fiber reinforced polymer matrix composites are a class of materials that offer high strength relative to their density. Furthermore, the mechanical properties can be tuned by selecting the orientation and arrangement of the fibers. This combination of properties makes polymer matrix composites an attractive materials group for lightweight structural applications in the transportation sector. Thermoset resin reinforced carbon fiber composites are of special interest, because the carbon fibers have a particularly high strength to density ratio as compared to other types of fibers, and because thermoset reins have increased stiffness and improved thermal resistance over thermoplastics.[1] Properly manufactured, carbon fiber composites have mechanical properties that rival steel, but have dramatically lower densities. Replacing traditional metal components with composite ones thus has the potential benefit of realizing significant weight savings, which in turn improve vehicle efficiency.

To form a carbon composite, a thermoset resin and its hardener are mixed together and infused into a fabric at a specified temperature and pressure. The resin is then allowed to cure, forming a covalently bonded network around the fibers of the fabric. Typically the cure reactions for thermoset resins are

exothermic. The temperature of the curing resin must therefore be controlled in order to compensate for the heat released during cure. The time that it takes to cure depends on the chemistry of the polymer system, as well as the processing conditions of system. There are few constraints on chemical diffusion or shrinkage for resin cured without additives. As a result the mechanical properties and cure kinetics of a given polymer system tend to be predictable with simple models [2]. When densely packed carbon fibers are added to the polymer, they significantly change the curing environment for the resin.

The physical presence of fibers can obstruct the free flow of the resin while it is still in liquid form. Carbon fibers also have a higher thermal conductivity than the resin, potentially resulting in a different temperature profile for resin curing in different regions of the composite. Finally, carbon fibers often have treatments that change the surface chemistry between the fiber and the resin for improved bonding characteristics. Together, these changes in the local environment of the resin during cure result in changes in the cure kinetics and final mechanical properties of the resin. Because the fibers also impede the movement of the curing matrix polymer, they can restrict cure shrinkage, which in turn can generate significant internal stresses and even induce microcracking of the matrix [3, 4]. In order to improve predictions of the mechanical behavior of a composite part, it is essential to develop better mechanical models that capture the effect of fibers on the cure behavior and final properties of the polymer matrix material.

One method to improve on existing mechanical models is to explicitly simulate the cure behavior of the resin within a composite and predict the variation in mechanical properties related to the presence of the fibers. The initial structure of the fibers and liquid resin are entered into the model along with constraints such as the temperature and pressure of the mold. Accurate materials characteristics of both the fibers and the resin are also required as input. Using the model one can then simulate the curing of the matrix including the heat evolved from the reaction and cure shrinkage. Simulating these effects in turn allows one to predict residual stresses in the matrix that result from the cure process [5-7]. In order for this type of model to work, it is critical to have an accurate model of the cure kinetics of the matrix polymer, and to know how the cure kinetics relates to the evolution of the mechanical properties of the matrix. Finally there must be a means of directly measuring real composite samples in order to refine the model and verify its predictions.

It is reasonable to believe that the *in situ* mechanical properties of the matrix polymer confined between fibers are not the same as those of the bulk, due to the complex geometry and difference in processing conditions due to the confinement by fibers in the composite. In fact, based on results from finite element modeling, Song et al. have proposed that the mechanical properties of an epoxy matrix cured in the presence of carbon fibers is significantly different from epoxy cured in bulk. [8] To test the hypothesis, and to provide input for improved finite element models, we measure the mechanical properties of an epoxy resin within a composite with high spatial resolution. Furthermore, to

accurately account for the thermal and chemical processing history of the matrix, we measure the thermo-mechanical properties of the epoxy during cure with high temporal resolution. In order to carry out these measurements, we have developed a new experimental approach, combining Brillouin and Raman light scattering techniques to measure the mechanical properties and chemical composition of a material.

1.2 Polymer Rheokinetics

The cure kinetics of a given polymer system are governed by transport and reaction processes. Typically, a resin monomer is mixed with a curing agent or catalyst that initiates polymerization. In the case of a resin and hardener system, each resin molecule can react with one or more hardener molecules. If both the resin and hardener molecules are bi-functional, the resulting polymer will consist of long chain molecules and will be a thermoplastic. If the two components are at a minimum bi-functional and at least one of the components can form three or more linking bonds, then the system has the ability to form crosslinks between the chains. These are called thermoset polymers. In the case of a monomer polymerized by a catalyst, the functionality of the monomer determines whether the resulting polymer will be a thermoset or thermoplastic. Typically the degree of cure (α) can be modeled using a reaction rate equation of the form:

$$\frac{d\alpha}{dt} = k(T) f(\alpha), \tag{1.1}$$

where the rate coefficient $k(T)$ typically exhibits an Arrhenius type temperature dependence,

$$k(T) = Ae^{\left(\frac{-E_a}{RT}\right)}, \quad (1.2)$$

A is a constant, E_a is the activation energy required for the reaction, R is the ideal gas constant, and T is the temperature of the system[2, 9-12]. The function $f(\alpha)$ depends on the nature of the polymerization reaction. It takes into account factors such as the number of bonds formed by the monomers, whether the bonds are reversible, and the reaction pathway by which the bonds are formed. Fundamentally, this type of reaction equation assumes that the monomers are free to move within some form of solvent, and their motion is unimpeded by the reaction. While this is clearly not the case for a resin that forms a rigid solid as result of curing, this type of model generally serves as a good approximation for cure behavior [2, 9, 10].

While modeling the cure kinetics of a resin has been given extensive consideration in the literature, many fewer approaches exist towards relating the degree of cure to mechanical characteristics of the polymer network. Two polymer networks composed of the same number of bonds can have significantly different configurations of those bonds. As a result the rigidity of the two networks will be different [13-16]. Historically, much work has been done on the subject of network connectivity [17-25]. For this purpose, connectivity is a statistical measure of how interconnected the elements of a network are. As more bonds are formed in a region of fixed volume, the probability of two network elements being connected by a series of bonds increases. Gelation occurs when the network structure spans its volume, thus achieving an infinite molecular weight

[2]. At this point the network structure is capable of supporting finite shear loads. This transition is readily observed using standard viscometry techniques.

Much research has been done on the prediction of the gelation point of polymer networks, as it is an important parameter in polymer molding and extrusion processes [13-15]. While gelation theory does reasonably well in connecting cure behavior to the viscosity of a polymer it does not yet fully describe the elastic moduli of the fully cured system. This is in part because to predict the elasticity of the network, more details must be known about the geometric structure of the network [13-15]. However, the network structure is not fully accounted for in typical gelation models. Furthermore, as the system transitions from a liquid to a solid, the standard techniques to measure visco-elastic properties change, making it difficult to capture the full cure behavior using one continuous series of measurements [2, 26]. As a result, models for the degree of cure, viscosity, and elastic properties of a polymer network tend to be empirically determined, and depend on the polymer system and the measurement techniques being used.[2] Because the measurement technique is an important factor in modeling visco-elastic properties as a result of cure, the most common techniques for measuring cure kinetics and mechanical properties of curing polymer systems are briefly outlined in the following.

1.3 Overview of Rheokinetic Measurement Techniques

To measure the degree of cure of a reacting system, there are two predominant approaches. The first is through calorimetry where the enthalpy of reaction is monitored over time. The second is chemical spectroscopy, where

chemical signatures of the network are observed optically during the cure process. Differential scanning calorimetry (DSC) is the most common calorimetric technique for observing cure kinetics. In a DSC experiment, a sample of known mass is placed into a calorimeter where its temperature is monitored via a thermocouple. The sample is compared to a standard with known thermal characteristics installed in an identical sample chamber. The calorimeter modulates the temperatures of both the sample and the standard. The calorimeter records the relative response of the sample to these modulations. The release of heat during polymerization can therefore be recorded, and the degree of cure is determined by the cumulative amount of the heat released by a sample as a function of time, compared to the total amount of heat released over the entire cure process [26, 27]. By careful modulation of the sample temperature it is often possible to find the heat of reaction for different processes in the cure reaction, and to monitor the heat capacity of the system as it changes with cure [27]. Together these data are useful in determining the rate coefficient of the cure model. DSC is a reasonably simple method and generally yields consistent results. However it is limited in the information that it provides about the underlying chemistry of the cure reaction. For example, due to steric hindrances imposed by the growing network structure a polymer network rarely incorporates all of the potentially reactable network sites of its monomer components. Because DSC only monitors the heat released by the system, on its own, it cannot determine the number of network bonds formed by the system.[28, 29]

Spectroscopic methods, on the other hand, use the optical absorption and emission spectra of a substance to measure changes in its chemistry. Typically a sample is illuminated by a light source of known character, and the light transmitted or scattered by the sample is analyzed. In IR and Raman spectroscopy for example, vibrations of molecular functional groups generate a characteristic spectrum of the sample. As the concentration of a functional group changes, it in turn changes the intensity of the related peaks in the sample's spectrum [30-34]. By monitoring changes in the spectrum during cure it is possible to determine then relative concentrations of different functional groups during the cure process. In this manner, spectroscopy can yield detailed information about the number and types of network bonds formed in a system [29, 35-38]. The major drawback to using spectroscopy to monitor cure behavior is that the spectra of polymer networks tend to consist of a large number of peaks due to the complexity of the polymer structure. It is not always trivial to determine which molecular structures give rise to each peak [29].

While chemical spectroscopy and calorimetry provide information about cure kinetics, they reveal little about the elastic properties of a system. One of the most common techniques to determine the visco-elastic properties of a polymer during the process of gelation is mechanical rheometry. Typically a sample is placed between parallel circular plates and an oscillating shear load is applied to the sample. A load cell measures the torque transmitted through the sample. From this data, the viscosity and shear modulus of the sample can be determined. Furthermore, by scanning through a range of oscillation frequencies,

the rate dependence of these properties can be determined [2]. Rheometry is widely used to capture gelation kinetics because the viscosity data that it collects is essential in engineering high throughput polymer molding applications. Rheometry is particularly sensitive to the gel point, which has also made it a tool of choice for studying network formation in polymers. In some cases it has been used as a method to approximate the cure kinetics of a polymer by measuring the relative change in the shear modulus over time [9-11]. In some systems this method correlates well with cure kinetic measurements made by using DSC, however it is at best an approximation of the true state of cure. It is difficult to conduct rheometric measurements beyond the gel point for especially rigid polymers [26]. Therefore, after gelation other techniques are typically used to determine the elastic properties of the polymer.

Ultrasonic spectroscopy is one technique that can be used to measure elastic properties beyond the gel point. Ultrasonic transducers are placed on opposite sides of a sample and sound waves are transmitted from one transducer to the other. Measuring the velocity and attenuation of the transmitted sound waves allows one to calculate the elastic moduli and structural relaxation rates of the sample [39, 40]. By properly orienting the transducers, both shear and longitudinal modes can be probed. Because the ultrasound transducers only impart very small deformations to the sample, it is possible to monitor the elastic properties of a curing sample well beyond the gel point.

All of the methods of mechanical characterization outlined so far have limited spatial resolutions, and as such are unsuitable for measuring the

mechanical properties of a polymer confined within micron scale regions of a composite. Furthermore, these methods require mechanical actuation of the material, which may have an effect on a developing network structure. The method we selected to measure the elastic properties of a polymer during cure is Brillouin light scattering. Unlike the previously described methods, Brillouin scattering is a non-contact, optical technique for measuring a substance's elastic properties with high spatial resolution. Furthermore, as an optical method, it can be coupled with other spectroscopic techniques that use the same wavelength of light, such as Raman spectroscopy. In this way it is possible to simultaneously measure changes in both the chemical structure, and the mechanical properties of a polymer within the same focal volume. Brillouin light scattering is similar to ultrasonic spectroscopy in that it measures the velocity and attenuation of sound waves in a sample. However rather than inducing the sound waves, Brillouin scattering measures existing, thermally excited sound waves in the sample. To do this, monochromatic light is used to illuminate the sample, and scattered light is collected and analyzed. Light scattered from thermal phonons in the sample is Doppler-shifted in frequency. Using the frequency shift it is possible to calculate the speed of sound, and from that the elastic modulus of the sample. Further details of this method will be covered in the next chapter. Because it is an optical technique, Brillouin scattering does not require any mechanical contact with the sample, and as such it can be used through the entire cure process and beyond gelation [40-43]. Furthermore, its spatial resolution is limited only by the wavelength of light used to illuminate the sample. Therefore, the mechanical

properties of very small (~1μm) features of a sample can be measured [44-49]. Combined, Brillouin and Raman light scattering is an ideal pair of techniques for probing the elastic properties of the matrix material between carbon fibers in a composite, and to determine the relationship between cure chemistry and the development of mechanical properties in a polymer network.

1.4 Thesis overview

In my research, I have studied the relationship between chemical cure kinetics and the development of the elastic moduli in thermoset polymers. The purpose of this work was to develop a method for measuring and subsequently modeling the modulus as a function of cure and time with the intent of incorporating the modulus-cure models into finite element simulations of curing composite materials. To experimentally measure the cure and mechanical properties of the polymers, I chose to use Raman and Brillouin light scattering. These two techniques are complementary for this purpose because they can share the same optical setup to provide concurrent information on the chemical and mechanical state of a polymer through out the entire cure process. Chapter 2 of this thesis presents a detailed overview of the theory and applications of these two methods. In Chapter 3, I apply the concurrent Raman-Brillouin scattering method to Dicyclopentadiene (DCPD) cured by ring opening metathesis polymerization (ROPM) with the aid of Grubs's catalyst. This is a polymer system of interest for developing self-healing composite materials. Furthermore, DCPD is a simple organic molecule with distinct Raman peaks associated with each of its reactive sites. This makes it an ideal test case for coupling Raman and Brillouin

methods to relate degree of cure to the elastic modulus. In Chapter 4, I apply the same methods to a system composed of the epoxy resin Epon 862 and the aliphatic amine hardener Epikure 9553. This system is used as a matrix polymer in carbon fiber composites, and as such is representative of the polymer systems that this analysis technique is meant to address. In Chapter 5, I use concurrent Raman and Brillouin scattering to survey different regions of a cross-sectioned carbon fiber composite in order to directly measure the effect that curing in the presence of carbon fibers has on the final mechanical properties of the same Epon 862 and Epikure 9553 epoxy system. Finally, Chapter 6 presents a conclusion in which the strengths and weaknesses of concurrent Raman-Brillouin scattering for this application are presented. Directions for future inquiry will be suggested based on the insights obtained from our research.

1.5 References

[1] FL Matthews,RD Rawlings, *Composite Materials: Engineering and Science* (Woodhead Publishing Limited, Cambridge, 1999).

[2] Halley PJ,Mackay ME. Chemorheology of thermosets-an overview. Polymer Engineering & Science 1996;36(5):593-609.

[3] Corden TJ, Jones IA, Jones DT,Middleton V. The mechanisms of interlaminar cracking in thick resin transfer moulded composite cylinders. Composites Part A: Applied Science and Manufacturing 1998;29(4):455-64.

[4] Lincoln JE, Morgan RJ,Shin EE. Fundamental investigation of cure-induced microcracking in carbon fiber/bismaleimide cross-ply laminates. Polymer Composites Polym Compos 2001;22(3):397-419.

[5] Heinrich C, Aldridge M, Wineman AS, Kieffer J, Waas AM,Shahwan K. The influence of the representative volume element (RVE) size on the homogenized response of cured fiber composites. Modelling Simul. Mater. Sci. Eng. 2012;20(7):075007.

[6] Heinrich C, Aldridge M, Wineman AS, Kieffer J, Waas AM,Shahwan KW. Generation of heat and stress during the cure of polymers used in fiber composites. International Journal of Engineering Science 2012;53(85-111.

[7] Heinrich C, Aldridge M, Wineman AS, Kieffer J, Waas AM,Shahwan KW. The role of curing stresses in subsequent response, damage and failure of textile polymer composites. Journal of the Mechanics and Physics of Solids 2013;61(5):1241-64.

[8] Song S, Waas AM, Shahwan KW, Xiao X,Faruque O. Braided textile composites under compressive loads: Modeling the response, strength and degradation. Composites Science and Technology 2007;67(15-16):3059-70.

[9] Malkin A,Kulichikhin S. Rheokinetics of curing. Polymer Compositions Stabilizers/Curing 1991;217-57.

[10] Malkin AY, Kulichikhin SG, Kerber ML, Gorbunova IY,Murashova EA. Rheokinetics of curing of epoxy resins near the glass transition. Polymer Engineering & Science 1997;37(8):1322-30.

[11] Reghunadhan Nair CP,Ninan KN. Rheological cure characterization of phosphazene-triazine polymers. Journal of Applied Polymer Science 2003;88(4):908-14.

[12] Zlatanic A, Dunjic B,Djonlagic J. Rheological study of the copolymerization reaction of acrylate-terminated unsaturated copolyesters with styrene. Macromolecular Chemistry and Physics 1999;200(9):2048-58.

[13] MF Thorpe, DJ Jacobs, NV Chubynsky,AJ Rader, in *Generic Rigidity of Network Glasses*, Ta Duxbury, Ed. (Kluwer Academic. Plenum Publishers, 1999), pp. 239-77.

[14] M.F. T. Rigidity percolation in glassy structures. J. Non-crystalline Solids 1985;76(109-16.

[15] Wilhelm J,Frey E. Elasticity of Stiff Polymer Networks. Phys. Rev. Lett. 2003;91(10)

[16] Wool RP. Rigidity percolation model of polymer fracture. J. Polym. Sci. B Polym. Phys. 2005;43(2):168-83.

[17] Flory PJ,Rehner J, John. Statistical Mechanics of Cross-Linked Polymer Networks I. Rubberlike Elasticity. The Journal of Chemical Physics The Journal of Chemical Physics J. Chem. Phys. 1943;11(11):512-20.

[18] Flory PJ,Rehner J, John. Statistical Mechanics of Cross-Linked Polymer Networks II. Swelling. The Journal of Chemical Physics The Journal of Chemical Physics J. Chem. Phys. 1943;11(11):521-6.

[19] Flory PJ. The Configuration of Real Polymer Chains. The Journal of Chemical Physics The Journal of Chemical Physics J. Chem. Phys. 1949;17(3):303-10.

[20] Flory PJ. Statistical Mechanics of Swelling of Network Structures. The Journal of Chemical Physics The Journal of Chemical Physics J. Chem. Phys. 1950;18(1):108-11.

[21] Flory PJ. Molecular Size Distribution in Three Dimensional Polymers. VI. Branched Polymers Containing A,ÄîR,ÄîBf-1 Type Units. Journal of the American Chemical Society 2002;74(11):2718-23.

[22] Flory PJ,Erman B. Theory of elasticity of polymer networks. 3. Macromolecules 2002;15(3):800-6.

[23] Rolfes H,Stepto RFT. A development of Ahmad-Stepto gelation theory. Makromol. Chem, Macromol. Symp. 1993;76(1-12.

[24] D Stauffer, A Conigllio,M Adam, in *Gelation and Critical Phenomena*, K Dusek, Ed. 1982), pp. 103-58.

[25] Stockmayer WH. Theory of Molecular Size Distribution and Gel Formation in Branched-Chain Polymers. J. Chem. Phys. 1943;11(2)(2):45.

[26] O'Brien DJ, Mather P,White S. Viscoelastic properties of an epoxy resin during cure. Journal of composite materials 2001;35(10):883.

[27] O'Brien DJ,White SR. Cure kinetics, gelation, and glass transition of a bisphenol F epoxide. Polymer Engineering & Science 2003;43(4):863-74.

[28] Merad L *et al.* In-situ monitoring of the curing of epoxy resins by Raman spectroscopy. Polymer Testing 2009;28(1):42-5.

[29] Yang YS,Lee LJ. Comparison of thermal and infrared spectroscopic analyses in the formation of polyurethane, unsaturated polyester, and their blends. Journal of Applied Polymer Science 1988;36(6):1325-42.

[30] Chike KE, Myrick ML, Lyon RE,Angel SM. Raman and Near-Infrared Studies of an Epoxy Resin. Appl. Spectrosc. Applied Spectroscopy Appl. Spectrosc. 1993;47(10):1631-5.

[31] Fischer M,Tran C. Evidence for kinetic inhomogeneity in the curing of epoxy using the near-infrared multispectral imaging technique. Anal. Chem 1999;71(5):953-9.

[32] Lyon RE, Chike KE,Angel SM. In situ cure monitoring of epoxy resins using fiber-optic Raman spectroscopy. Journal of Applied Polymer Science 1994;53(13):1805-12.

[33] Mertzel E,Koenig J. Application of FT-IR and NMR to epoxy resins. Epoxy Resins and Composites II 1986;73-112.

[34] Tran C. Visualising chemical composition and reaction kinetics by the near infrared multispectral imaging technique. Journal of Near Infrared Spectroscopy. 2000;8(89-102.

[35] Aust JF, Booksh KS, Stellman CM, Parnas RS,Myrick ML. Precise Determination of Percent Cure of Epoxide Polymers and Composites via Fiber-Optic Raman Spectroscopy and Multivariate Analysis. Appl. Spectrosc. Applied Spectroscopy Appl. Spectrosc. 1997;51(2):247-52.

[36] Barnes S, Brown E, Corrigan N, Coates P, Harkin-Jones E,Edwards H. Raman spectroscopic studies of the cure of dicyclopentadiene (DCPD). Spectrochim Acta A Mol Biomol Spectrosc 2005;61(13-14):2946-52.

[37] Meyer F, Sanz G, Eceiza A, Mondragon I,Mijovi J. The effect of stoichiometry and thermal history during cure on structure and properties of epoxy networks. Polymer 1995;36(7):1407-14.

[38] Xu L, Fu JH,Schlup JR. In Situ Near-Infrared Spectroscopic Investigation of the Kinetics and Mechanisms of Reactions between Phenyl Glycidyl Ether (PGE) and Multifunctional Aromatic Amines. Industrial & Engineering Chemistry Research 1996;35(3):963-72.

[39] Matsukawa M,Nagai I. Ultrasonic characterization of a polymerizing epoxy resin with imbalanced stoichiometry. The Journal of the Acoustical Society of America 1996;99(4):2110-5.

[40] Yamura H, Matsukawa M, Otani T,Ohtori N. Brillouin scattering study on the elastic properties of epoxy adhesive layer. Jpn. J. Appl. Phys., Part 1999;1(38):3175.

[41] Caponi S, Corezzi S, Fioretto D, Fontana A, Monaco G,Rossi F. Raman-Scattering Measurements of the Vibrational Density of States of a Reactive Mixture During Polymerization: Effect on the Boson Peak. Physical Review Letters Physical Review Letters Phys. Rev. Lett. 2009;102(2):027402-4.

[42] Philipp M, Müller U, Riobóo R, Baller J, R ,. Interphases, gelation, vitrification, porous glasses and the generalized Cauchy relation: epoxy/. New Journal of Physics 2009;

[43] R Sanctuary, M Philipp, J Kieffer, U Muller, W Possart,JK Kruger, *Trans-Interfacial Polymerization and Matter Transport Processes in Epoxy-Alumina Nanocomposites Visualized By Scanning Brillouin Microscopy* Univ

Luxembourg, Lab Phys Mat, Grand Duchy, Luxembourg roland.sanctuary@uni.lu, 2010), pp. 8396-404.

[44] Müller U *et al.* Acoustic profilometry of interphases in epoxy due to segregation and diffusion using Brillouin microscopy. New Journal of Physics 2008;10(2):023031.

[45] Philipp M *et al.* Mixing behavior and interphase formation in the diethylene triamine-water system studied by optical imaging and spatially resolved Brillouin scattering. J Phys Chem B 2009;113(38):12655-62.

[46] Possart W *et al.* Formation and structure of epoxy network interphases at the contact to native metal surfaces. Comptes rendus-Chimie 2006;9(1):60-79.

[47] Scarcelli G,Yun S. Confocal Brillouin microscopy for three-dimensional mechanical imaging. Nat Photonics 2007;2(39-43.

[48] Scarcelli G,Yun SH. In vivo Brillouin optical microscopy of the human eye. Opt. Express Optics Express Opt. Express 2012;20(8):9197-202.

[49] Scarcelli G, Kling S, Quijano E, Pineda R, Marcos S,Yun SH. Brillouin Microscopy of Collagen Crosslinking: Noncontact Depth-Dependent Analysis of Corneal Elastic Modulus. Investigative Ophthalmology & Visual Science 2013;54(2):1418-25.

Chapter 2

Brillouin and Raman Light Scattering Theory

2.1 Brillouin Light Scattering Theory

Most methods of characterizing the mechanical properties of materials require damaging or destroying the sample. However, this is not always desirable, and we turn to nondestructive techniques, typically involving sound or light. Thermal motion of atoms and molecules within a material results in fluctuations of the local density and dielectric constant of the material. Light traveling within the material is effected by these changes in the dielectric constant and is scattered as a result of the changing interactions. The fluctuations in dielectric properties associated with acoustic phonons induce scattering. Furthermore, the plane-wave nature of these phonons enforces a diffraction condition on the scattered light. Only the portion of the scattered light meeting the diffraction condition will continue to propagate. All other light scattered from the phonon will be eliminated due to destructive interference. It is therefore possible to establish the wavevector of the selected phonon by measuring the angle by which the light is scattered, as shown in Figure 2.1. In an isotropic medium, the phonon wavevector ($\boldsymbol{q}$) is defined as the difference between the wavevectors of the incident ($\boldsymbol{k_s}$) and scattered light ($\boldsymbol{k_i}$):

$$\pm \boldsymbol{q} = (\boldsymbol{k}_s - \boldsymbol{k}_i). \tag{2.1}$$

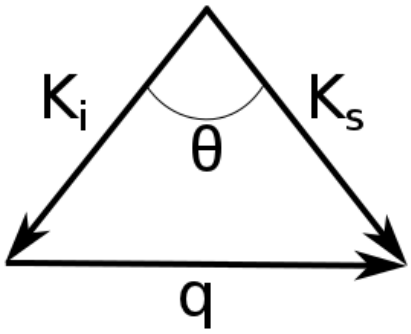

Figure 2.1 Schematic of light scattering. The incident and scattered light wavevectors are k_i and k_s, the phonon wavevector is q, and the scattering angle θ

The + sign refers to the case where the phonon is absorbed (anti-Stokes) and the – sign denotes the emission of a phonon (Stokes). Because the velocity of sound is much smaller than the velocity of light, it is a good approximation to treat the magnitudes of $\boldsymbol{k_s}$ and $\boldsymbol{k_i}$ as being equal:

$$|\boldsymbol{k_s}| = |\boldsymbol{k_i}| = \frac{n}{\lambda_0}, \tag{2.2}$$

Here n is the index of refraction of the medium, and λ_0 is the wavelength of the light in a vacuum. As Figure 2.1 shows, it is easy to calculate the magnitude of **q** using the scattering angle θ, the index of refraction and the wavelength of the scattered light:

$$|\boldsymbol{q}| = 2|\boldsymbol{k_s}| sin\left(\frac{\theta}{2}\right) = \frac{2n}{\lambda_0} sin\left(\frac{\theta}{2}\right). \tag{2.3}$$

The phenomenon when the photons are scattered elastically is called Rayleigh scattering. The photons can also exchange momentum with the acoustic phonons. When this happens, the scattered light is Doppler shifted according to the velocity of sound of the medium. This case is called Brillouin scattering, and is named after Léon Brillouin who first predicted it in 1922. The

shape of the light scattering spectrum is called the dynamic structure factor. For an idealized monoatomic liquid, it can be calculated using a generalized hydrodynamic formalism. The calculation depends on the viscoelastic and thermodynamic properties of the scattering medium. The resulting normalized scattering intensity is a function of the scattering wavevector, q, and frequency, ω, and is composed of three Lorentzian terms: [1, 2]

$$\frac{S(q,\omega)}{S(q)} = \frac{2(\gamma-1)}{\gamma}\frac{q^2\left(\kappa/\rho_0 c_p\right)}{\omega^2+\left(q^2\left(\kappa/\rho_0 c_p\right)\right)^2} + \frac{1}{\gamma}\left(\frac{q^2\Gamma}{(\omega+\nu_{\mathrm{L}}q)^2+(q^2\Gamma)^2}+\frac{q^2\Gamma}{(\omega-\nu_{\mathrm{L}}q)^2+(q^2\Gamma)^2}\right), \tag{2.4}$$

where $\gamma = c_p/c_v$, $\Gamma = (1/2)\left[\eta'(\omega)/\rho_0 + \left(\kappa/\rho_0 c_p\right)(\gamma-1)\right]$, ρ_0 is the average density, and c_p is the heat capacity at constant pressure. The coefficient $\eta'(\omega)$ is the dynamic viscosity and $(\kappa/\rho_0 c_p)$ is the thermal diffusivity of the medium. The first term describes the Rayleigh scattered component of the spectrum, while the second and third terms are due the Stokes and anti-Stokes components of Brillouin scattering. In this case, only longitudinal phonons cause scattering, and v_L is the longitudinal sound velocity. The light scattered from these longitudinal phonons retains its polarization relative to the scattering plane. For materials composed of optically anisotropic molecules, a depolarized component of the spectrum is introduced. That is to say, in addition to the previously described spectrum, there is a component of the scattered light with its polarization rotated by 90^{o} relative to the incident light. Figure 2.2 illustrates these differences in polarization. The exact structure factor for the depolarized component is difficult

to calculate. However, the relevant feature of the depolarized scattering component is the addition of another Brillouin peak doublet that depends on the shear properties of the medium. These peaks can be approximated as Lorentzian in shape, with their centers at ± $v_s q$, where v_s is the shear wave velocity. The width of these peaks is determined by the shear and reorientational relaxation frequencies of the molecules within the material.[3]

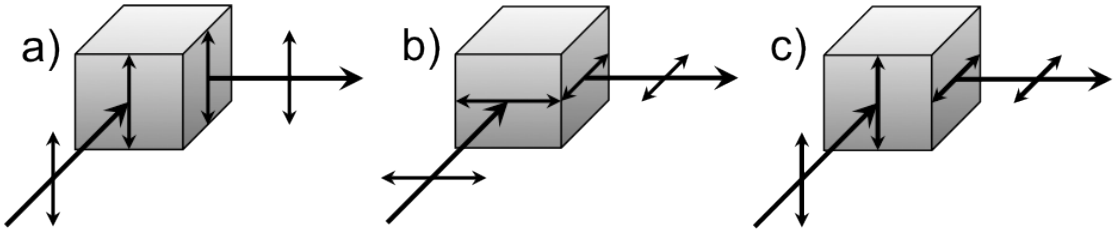

Figure 2.2 Schematic of incident and scattered light polarizations: a) VV, b) HH, c) VH. The double pointed arrows denote the polarization, and the single pointed arrows denote the direction of light propagation.

The intensities of the polarized and depolarized components of the Brillouin spectrum are determined by the magnitude of the dielectric constant change as a result of elastic deformations. A linear combination of the elements of the elastic strain tensor can be used to describe the changes in the dielectric constant of a material. The coefficients of this combination are called the elasto-optical or Pockels coefficients P_{ij}.[4] The Brillouin scattering intensities depend on these coefficients as well as the scattering angle. The power $I_{\alpha\beta}$ of light scattered by longitudinal acoustic phonons from polarization α to polarization β per unit solid angle is:

$$I_{VV} = I_0 V_{sc} \pi^2 kT \frac{\epsilon^4}{\lambda_0^4} \frac{|P_{12}|^2}{\rho_0 v_L^2}, \tag{2.5}$$

$$I_{HH} = I_0 V_{sc} \pi^2 kT \frac{\epsilon^4}{\lambda_0^4} \frac{1}{\rho_0 v_L^2} |P_{44} + (P_{12} + P_{44}) cos\theta|^2, \quad (2.6)$$

Likewise for transverse (shear) phonons, the scattering power is:

$$I_{VH} = I_{HV} = I_0 V_{sc} \pi^2 kT \frac{\epsilon^4}{\lambda_0^4} \frac{|P_{44}|^2}{\rho_0 v_s^2} cos^2\left(\frac{\theta}{2}\right), \quad (2.7)$$

The subscripts *V* and *H* refer to vertical and horizontal polarization relative to the scattering plane. I_0 is the incident light intensity, V_{sc} is the scattering volume, and kT is the thermal phonon energy. The dielectric constant at the laser frequency is ε, which is also equal to n^2. By combining the equation for dynamic structure factor with the equations governing the scattering intensity, we now have a detailed description of the Brillouin spectrum from which we can extract useful information about material properties.

2.1.1 Interpretation of the Brillouin spectrum

The most apparent features of the Brillouin spectrum are the two Lorentzian doublets corresponding to scattering by the longitudinal and transverse phonons. An example Brillouin spectrum is shown in Figure 2.3 The frequency by which these peaks are shifted from the central Rayleigh peak can be used to determine the adiabatic elastic properties of a material. We will denote the frequency corresponding to the peak centers as $\Delta\omega_L$ and $\Delta\omega_s$ for the longitudinal and shear peaks respectively. Inspection of the dynamic structure factor reveals that these peak centers correspond to ± $v_T q$, and ± $v_s q$. For a known scattering angle and index of refraction, we can therefore calculate the phonon velocity associated with both modes according to:

$$v = \frac{\Delta\omega}{|\boldsymbol{q}|} = \frac{\lambda_0 \Delta\omega}{2n\sin\left(\frac{\theta}{2}\right)}, \tag{2.8}$$

In this equation we dropped the subscript from *v* and *Δω* because the calculation is the same for both modes.

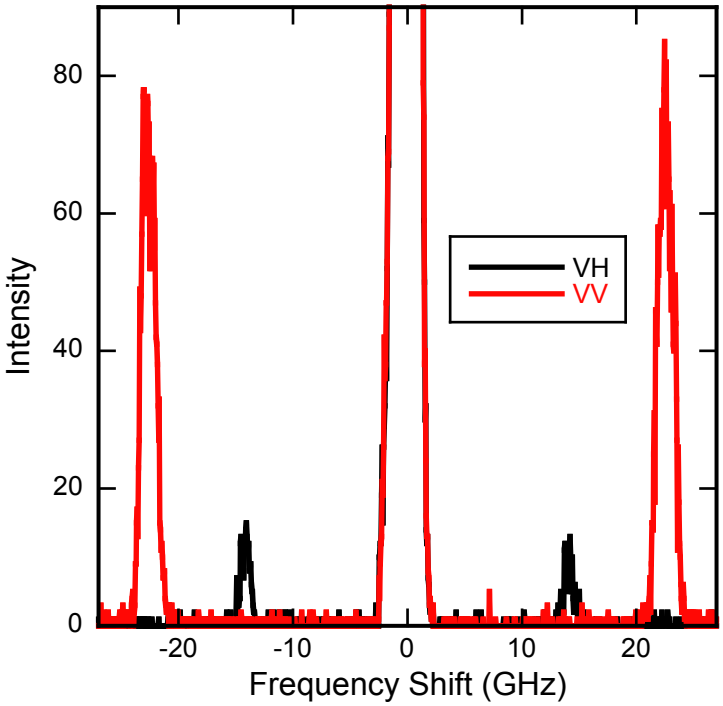

Figure 2.3 Example Brillouin spectrum with both VV and VH polarized components shown

Assuming that the mass density ρ_0 of a sample is known, the elastic modulus associated with each phonon probed can be determined using the sound velocity for that phonon.[5, 6] For Brillouin scattering, this means we can calculate the longitudinal modulus (*M*), and the shear (transverse) modulus (*G*) for a given sample using:

$$M = \rho_0 v_L^2 = \rho_0 \left(\frac{\lambda_0 \Delta\omega_L}{2n\sin\left(\frac{\theta}{2}\right)} \right)^2, \tag{2.9}$$

$$G = \rho_0 v_s^2 = \rho_0 \left(\frac{\lambda_0 \Delta\omega_S}{2n\sin\left(\frac{\theta}{2}\right)} \right)^2, \quad (2.10)$$

If the sample being measured generates a longitudinal peak as well as a measureable shear peak, the Young's modulus (*E*), bulk modulus (*K*), and the Poisson's ratio (*v*) can be calculated according to the following relations:

$$E = \frac{G(3M - 4G)}{M - G}, \quad (2.11)$$

$$K = M - \frac{4G}{3}, \quad (2.12)$$

$$\nu = \frac{M - 2G}{2M - 2G}, \quad (2.13)$$

In liquids where there is no appreciable shear modulus, the bulk modulus is the same as the longitudinal modulus. The ability to determine these values depends on the scattering angle used for the measurements. The shear component of the scattering spectrum, I_{VH}, becomes zero when the scattering angle is 180°. In this scattering configuration only the longitudinal modulus can be determined. An example data set of all four elastic moduli as measured concurrently by Brillouin scattering is shown in Figure 2.4. In this case, a highly crosslinked epoxy sample was observed over a range of temperatures. As the temperature is increased the epoxy softens, and the moduli decrease accordingly.

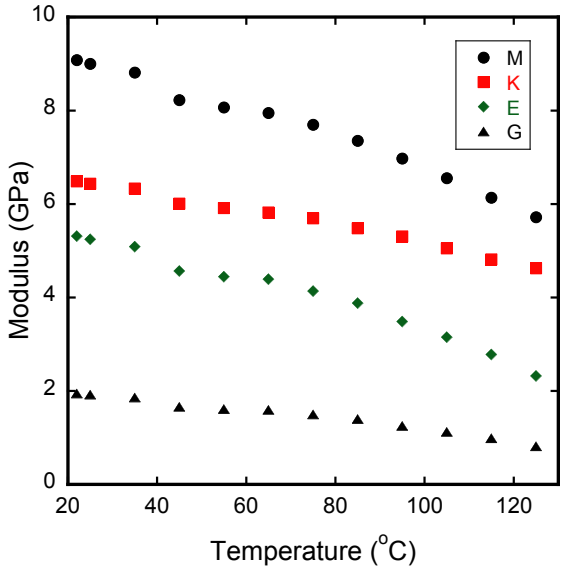

Figure 2.4 Elastic moduli of an epoxy sample as a function of temperature

It is important to note that the moduli measured by this method represent the high frequency (adiabatic) modulus. The vibrational modes being probed by Brillouin scattering occur much faster than typical thermal transport rates. Structural relaxations therefore occur on a slower timescale than the scattering phenomenon. As a result, Brillouin scattering measurements of viscous or visco-elastic materials will tend to produce much larger elastic moduli than a conventional tensile test would. This effect is minimized in very stiff, crystalline materials, which undergo little or no relaxation.

The widths of the Brillouin peaks are governed by transport and relaxation properties of the medium. In principal, the frequency dependent kinematic viscosity, ν'(ω) can be calculated from the widths and intensities of the Brillouin and Rayleigh peaks using the formula:[2]

$$(2.14) \qquad \nu'(\omega) = \frac{1}{|\boldsymbol{q}|^2}\left(\Gamma_{BL} - \frac{\Gamma_R I_R}{4 I_{BL}}\right),$$

Where Γ_{BL} and Γ_R are the full widths at half maximum of the longitudinal Brillouin and Raleigh peaks respectively. Likewise I_{BL} and I_R are the integrated areas of the longitudinal Brillouin and Rayleigh peaks. The ratio $I_R/4I_{BL}$ is generally small, on the order of 10^{-2}. Furthermore the width of the Rayleigh peak tends to be much narrower than that of the Brillouin peak. As a result the second term in brackets tends to be smaller than the variation in the experimental data and can be neglected from calculations of the viscosity. Therefore the kinematic viscosity of the material can be reasonably described using only the scattering wavevector and the measured width of the longitudinal Brillouin peak:[2]

$$\nu'(\omega) = \frac{\Gamma_{BL}}{|\boldsymbol{q}|^2}, \tag{2.15}$$

In practice, this measurement is more difficult than it appears here, because the optical configuration of the experiment introduces Gaussian broadening of the elements of the Brillouin spectrum. Great care must be taken to first determine the broadening function of the experimental setup in order to deconvolute the experimental broadening from the true Brillouin spectrum. Despite these difficulties, the width of the Brillouin peak serves as a good qualitative indicator for the changes in the viscosity of a material under observation.

The intensity of the polarized and depolarized components of the Brillouin spectrum can be used to directly measure the elasto-optic properties of the material. It is important to know these properties when designing optical components that may experience applied stresses in their regular working environments, as is the case with optical fibers. When light passes through a

stressed material, the electromagnetic components of the light experience different refractive indices relative to the two principal stress directions. The difference in refractive indices results in a relative phase retardation between the two components. The degree of retardation (*Δ*) is given by:

$$\Delta = \frac{n^3}{4G} C(\sigma_1 - \sigma_2), \tag{2.16}$$

where σ_1 and σ_2 are the first and second principal stresses, and C is known as the stress-optic coefficient. C depends on the value of the elasto-optic coefficient P_{44} according to:[7]

$$C = \frac{n^2}{4G} P_{44}, \tag{2.17}$$

To calculate the value of P_{44} from a Brilouin scattering experiments, one must first calculate P_{12}. The Brillouin scattering intensity of an arbitrary sample must be calibrated against that of a known standard with the same scattering geometry in order to calculate P_{12}. Generally, the standards used for this measurement have been toluene and SiO_2.[4, 8, 9] The relevant properties of these standards are summarized in Table 2.1. Using the Brilliouin scattering intensities of both the sample and the standard, the value of P_{12} can be calculated according to:

$$P_{12}^{smpl} = \left(\frac{I_{smpl}}{I_{std}}\right)^{\frac{1}{2}} \left(\frac{\rho_{smpl}}{\rho_{std}}\right)^{\frac{1}{2}} \left(\frac{v_L^{smpl}}{v_L^{std}}\right) \left(\frac{n_{std}}{n_{smpl}}\right)^4 P_{12}^{std}, \tag{2.18}$$

Depending on the relative absorptions and indices of refraction of the sample and standard, it may be necessary to include corrections for the attenuation of scattered light within the sample, and for differences in the solid angle over which the scattered light is collected.

Standard	Formula	Density (g/cm^3)	n	P_{12}
Toluene	C_7H_7	0.87	1.497	0.318
Quartz Glass	SiO_2	2.21	1.458	0.286

Table 2.1 Properties of the standards used to calibrate the intensity measurement of Brilouin spectra

Once the value of P_{12} is known, P_{44} can be calculated by comparing the intensities of the polarized and depolarized components of the Brillouin spectrum. From the equations describing the scattering intensity of the Brillouin spectrum we can see that for a 90-degree scattering angle, I_{VV} and I_{VH} each depend only on one of the two elasto-optic coefficients:

$$I_{VV} \propto \frac{P_{12}^2}{\rho v_L^2}, \tag{2.19}$$

$$I_{VH} = I_{HV} \propto \frac{P_{44}^2}{2\rho v_s^2}, \tag{2.20}$$

From here we can see that the ratio of P_{44} to P_{12} is easily calculated:

$$\frac{P_{44}}{P_{12}} = \frac{v_s}{v_L}\sqrt{\frac{2I_{VH}}{I_{VV}}}, \tag{2.21}$$

Combining this ratio with the previously determined value of P_{44} yields the following expression for P_{12}:

$$P_{44} = P_{12}\frac{v_s}{v_L}\sqrt{\frac{2I_{VH}}{I_{VV}}}, \tag{2.22}$$

Finally the relative sign of P_{12}/P_{44} can be calculated by comparing the scattering intensities of the polarized and depolarized components of the spectrum for scattering angles around 90-degrees. The ratio of the I_{HH} and I_{VH} scattering intensities depends on scattering angle according to:

$$\frac{I_{HH}}{I_{VH}} \propto \left| \frac{P_{44} + (P_{12} + P_{44})cos\theta}{P_{44}cos\left(\frac{\theta}{2}\right)} \right|^2, \tag{2.23}$$

Taking the derivative of this ratio with respect to the scattering angle yields:

$$\frac{\partial}{\partial\theta}\left(\frac{I_{HH}}{I_{VH}}\right) \propto -\left(\frac{2P_{12}}{P_{44}} + 1\right) \approx -\frac{2P_{12}}{P_{44}}, \tag{2.24}$$

The final approximation is made because generally $|2P_{12}/P_{44}| \gg 1$.[4] Therefore by measuring the slope of I_{HH}/I_{VH} as a function of the scattering angle, the relative sign of P_{12}/P_{44} can be determined. Figure 2.5 (a) shows the measured values of P_{12} and P_{44} for a series of lead phosphate glass compositions. The stress optic coefficient in figure 2.5 (b) is calculated from the P_{ij} values. Materials with a stress-optic coefficient near zero are of particular interest in the development of optical fibers.

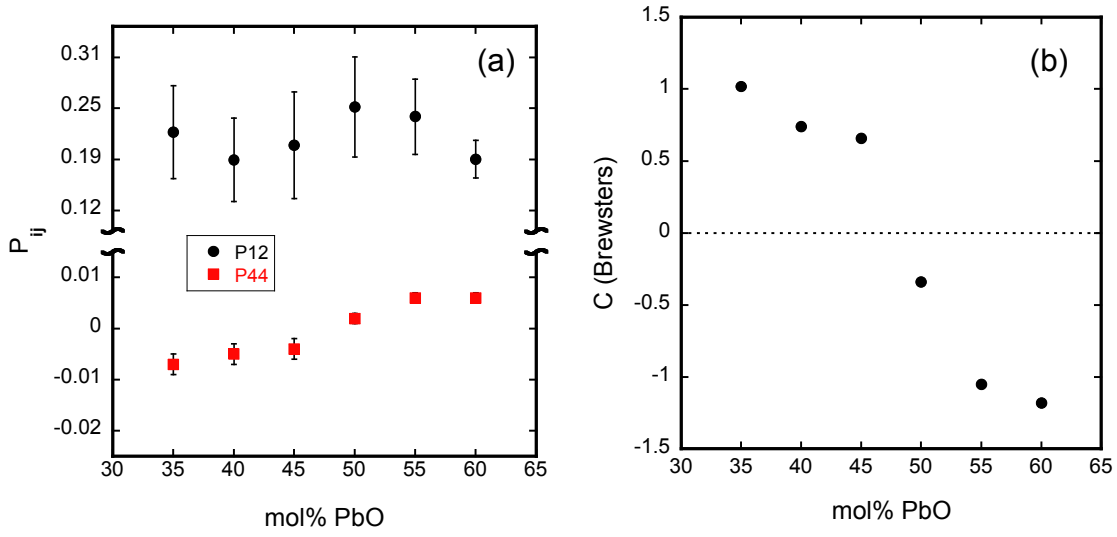

Figure 2.5 (a) Elasto-optic coefficients measured for different compositions of (x)PbO-(1-x)P_2O_5 glass, (b) The stress optic coefficient of the same series as calculated from the Brillouin scattering measurements

2.1.2 Brillouin Scattering Geometries

While theoretically scattering can be done using arbitrary scattering angles, and sample geometries, it can quickly become cumbersome to assemble an optical path with arbitrary scattering angles, and to calculate desired materials properties from the resulting spectra. Experimentally, most Brillouin scattering experiments are done using a handful of scattering geometries. These scattering geometries take advantage the relationship between scattering angle and scattering power as described above, as well as sample geometries that make calculating the true scattering angle (θ) within the sample much easier. Several of the most common scattering geometries are outlined below.

The most basic scattering geometry is known as 180 degree or backscattering. In this geometry the incident and scattered light pass through the same optics to and from the sample [Figure 2.6]. The angle of incidence with the sample does not matter, as the optical path of incident and scattered light is the same. The magnitude of the wavevector probed by this configuration is:

$$|\boldsymbol{q}(180°)| = \frac{2n}{\lambda_0}, \tag{2.25}$$

This is the largest **q** vector that can be measured by any scattering geometry. The magnitude of **q** makes it easier to probe samples with low densities or low elastic moduli. The major drawback to the backscattering geometry is that shear modes cannot be probed in this way.

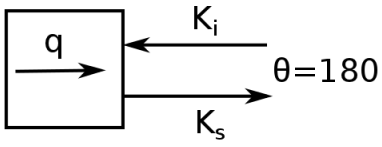

Figure 2.6 Schematic of backscattering geometry

The next common configuration is 90-degree scattering [figure 2.7]. In this geometry the incident and scattered light enter and exit the sample normal to the sample surface, and perpendicular to one another. The magnitude of **q** for this geometry is:

$$|\boldsymbol{q}(90°)| = \frac{n\sqrt{2}}{\lambda_0}, \tag{2.26}$$

While in principal any sample geometry that provides symmetric surfaces at 90° to each other will work for this geometry, in general samples are square in profile. Because the incident and scattered light are normal to the sample surfaces, the optical paths are not skewed by the index of refraction of the sample, thus the incident and scattered paths are the same inside and outside of the sample, and θ = 90. Furthermore, the shear component of the spectrum is maximized in intensity for this geometry.

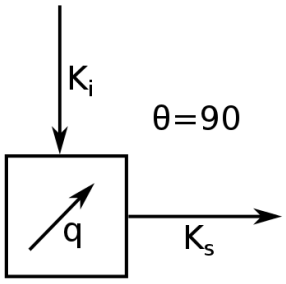

Figure 2.7 Schematic of 90degree scattering geometry

Platelet geometry requires that the sample be transparent and have parallel faces which bisect the scattering angle [figure 2.8]. This configuration takes advantage of the symmetry of the angles of the incident and scattered light with respect to the sample surface in order to eliminate the index of refraction from the calculation of the magnitude of **q**. The scattering wavevector in this geometry is in the plane of the sample, and its magnitude is given by:

$$|\boldsymbol{q_P}| = \frac{2n}{\lambda_0} sin\left(\frac{\theta'}{2}\right), \tag{2.27}$$

Assuming that the sample is in air, applying Snell's law gives us:

$$sin\left(\frac{\theta}{2}\right) = nsin\left(\frac{\theta'}{2}\right), \tag{2.28}$$

Which, when substituted back into the equation for $|\mathbf{q_p}|$ yields:

$$|\boldsymbol{q_P}| = \frac{2}{\lambda_0} sin\left(\frac{\theta}{2}\right), \tag{2.29}$$

Which is independent of the index of refraction. For the practical purpose of constructing a suitable beam path, a 90° scattering angle is most commonly used for platelet geometry. In this case the magnitude of the wavevector is:

$$|\boldsymbol{q_P}| = \frac{\sqrt{2}}{\lambda_0}. \tag{2.30}$$

Eliminating the need to know the index of refraction is particularly useful in situations where the refractive index is difficult to measure. This can be the case as during structural transitions within a sample, or in cases where *n* is too large to be measured by common refractometers.

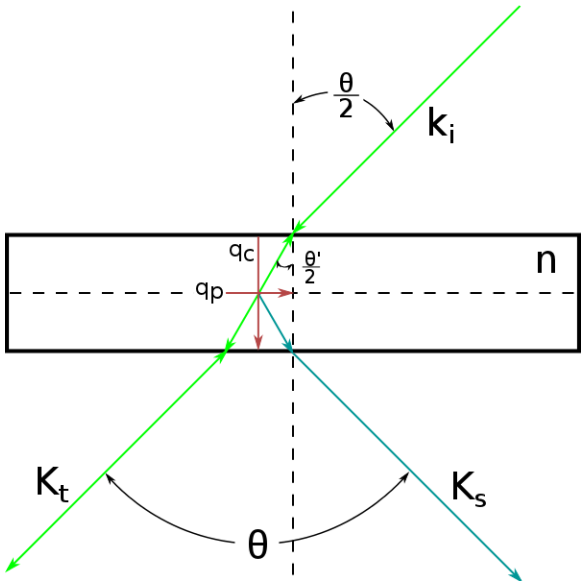

Figure 2.8 Schematic of platelet and platelet compliment scattering geometries

When the platelet geometry is configured, the light transmitted through the sample can be reflected back on its path, thus creating a second complimentary scattering geometry as shown in Figure 2.8. We call this geometry platelet compliment. In this geometry the wavevector probed is perpendicular to the plane of the sample, and the index of refraction is not canceled out by symmetry. In this geometry the magnitude of $\boldsymbol{q}$ is:

$$|\boldsymbol{q_c}| = \frac{2n}{\lambda_0}\left(1 - \frac{1}{n^2} sin^2\left(\frac{\theta}{2}\right)\right)^{\frac{1}{2}}. \tag{2.31}$$

If the sample is an isotropic material then the speed of sound is the same in all directions i.e. $v_p = v_c$, and as a result:

$$\frac{\Delta\omega_p}{|\boldsymbol{q_p}|} = \frac{\Delta\omega_c}{|\boldsymbol{q_c}|}, \tag{2.32}$$

where the subscripts p and c denote the platelet and compliment geometries. We can then substitute in the expressions for $\boldsymbol{q_p}$ and $\boldsymbol{q_c}$ and solve to find an expression for the index of refraction based entirely on the Brillouin spectrum:

$$n = \sqrt{\left(\left(\frac{\Delta\omega_c}{\Delta\omega_p}\right)^2 + 1\right) sin^2\left(\frac{\theta}{2}\right)}, \quad (2.33)$$

Since platelet geometry is generally used when it is difficult to determine a sample's index of refraction, this complimentary geometry can be a particularly useful tool for finding the value of *n*. Figure 2.9 shows the index of refraction of an epoxy sample as a function of degree of cure, as measured using the platelet and platelet compliment geometries. It is important to measure the elastic properties using the platelet geometry because the index changes along with the elastic properties of the epoxy.

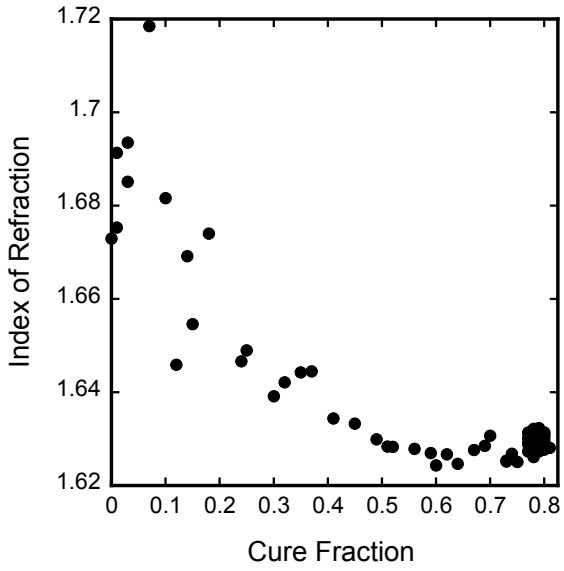

Figure 2.9 The index of refraction of a an epoxy sample as a function of cure

2.2 Theory of Raman Light Scattering

Like Brillouin scattering, Raman scattering is an inelastic light scattering phenomenon in which light interacts with a material and either absorbs or excites vibrations in the material. Unlike Brillouin scattering, which occurs on the scale of

local density fluctuations, the vibrations associated with Raman scattering occur on the scale of molecular bonds.

Vibrations of a molecular structure induce oscillations in the dipole moment of the molecule. The oscillating electromagnetic field of a photon can interact with the oscillating dipole moment, resulting in scattering. When a molecule absorbs a photon, the molecule will enter a higher and unstable energy state. Shortly after entering this unstable state, the molecule will transition back to a lower energy stable state and radiate a photon. If the energy of the absorbed photon corresponds to energy of a higher electronic state of the molecule, this process is called fluorescence. If the energy of the photon falls between the possible electronic transitions, there are four other possible outcomes as outlined in figure 2.10. If the higher energy level happens to correspond to a stable vibrational mode of the molecule, no photon will be emitted. This case is called infrared (IR) absorption. If the excited state is unstable, the molecule may return to its original state and the radiated photon will have the same energy as the absorbed photon. This is the elastic case called Rayleigh scattering. Furthermore, the molecule could return to a stable vibrational energy state higher or lower than its initial state. These cases are known as Raman scattering. In the case where the molecule returns to a lower energy state, the emitted photon will have greater energy than the incident photon and this case is called anti-Stokes scattering. In the opposite case, the emitted photon will have a lower energy, and the process is called Stokes scattering. The energy exchanges associated with

Raman scattering are larger than those observed for Brillouin scattering, with relative frequency shifts on the order of terahertz as opposed to gigahertz.

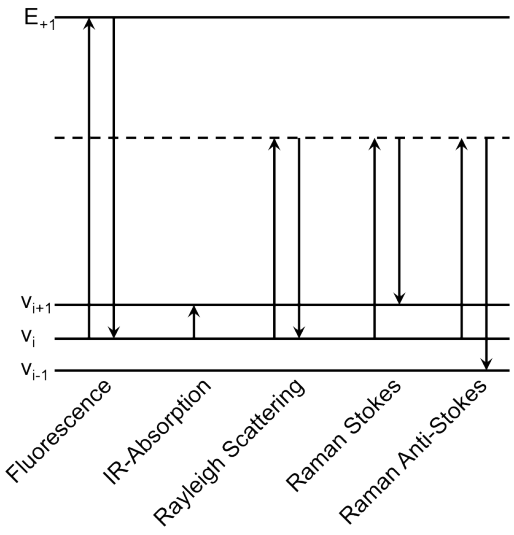

Figure 2.10 Schematic of the possible energy level transitions in molecular light scattering

A typical Raman spectrum is composed of a number of peaks with different energies. Each peak corresponds to a specific molecular vibration and a specific vibrational frequency. The structure of a molecule determines the number of peaks in its Raman spectrum. An organic molecule composed of *n* atoms will have 3*n* possible vibrational modes. Three of these modes correspond to pure linear translations of the molecule's position. Three more modes correspond to coordinated rotation of the entire molecule. In both of these cases the dipole moment of the molecule remains unchanged, and as such, they cannot support Raman scattering.[10] Figure 2.11 shows an example of the possible vibrations of a simple three-atom molecule. For the remaining 3*n*-6 modes, the eligibility for Raman scattering is determined by the manner in which the dipole moment of the molecule is. Only vibrational modes that change the

polarizability of the molecule can give rise to Raman scattering, and considered "Raman-active" modes. Molecular symmetry can further reduce the number of observable modes, as symmetrically identical vibrations have the same energies.

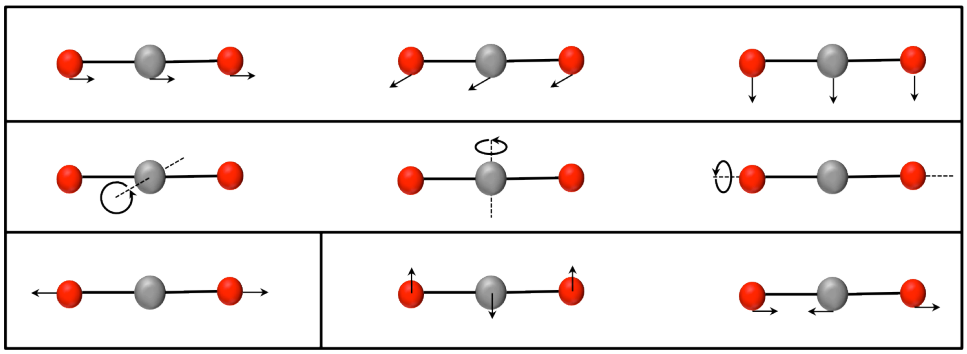

Figure 2.11 The nine possible molecular motions of a CO_2 molecule: Translations (top) Rotations (middle) and vibrations (bottom). Only the symmetric stretch mode of CO_2 (bottom left) is Raman active according to the polarizability selection rule.

While the structure of the molecule determines the number of Raman modes that can be excited, it does not necessarily yield any information about the frequencies of those modes. Instead, the mass of the vibrating atoms and the stiffness of the bond between them determines their frequency of oscillation. The vibrating atoms can be modeled classically as a simple harmonic oscillator joined by a spring. Hooke's law relates the atomic masses and the force constant of the bond to the frequency of oscillation (ν) according to:

$$\nu = \frac{1}{2\pi}\sqrt{\frac{f\left(M_x + M_y\right)}{M_x M_y}}, \tag{2.34}$$

where is the speed of light, *f* is the force constant of the bond, and M_x and M_y are the masses of the oscillating atoms.[11] Because Raman measurements analyze the change in energy of the scattered light, Raman spectra are presented in terms of the scattered light's relative wavenumber. The relative wavenumber Δω

of light scattered from an initial wavelength of λ_0 to a new wavelength λ_R is given by:

$$\Delta\omega = \omega_0 - \omega_R = \frac{1}{\lambda_0} - \frac{1}{\lambda_R}, \quad (2.35)$$

The relative wavenumber is particularly useful in understanding the modes of vibration because, unlike the shift in wavelength, it is directly proportional to the vibrational frequency according to: $\Delta\omega = \nu/c$, where c is the speed of light.[12]

The harmonic oscillator model works surprisingly well for predicting the stretching modes between atoms in simple molecules. However, the spectrum of more complex molecules will deviate significantly from the simple Hooke's law prediction as a result of coupling between other modes at similar frequencies, as well as with the overtones of lower frequency modes. Generally, a Raman spectrum can be broken into regions that contain characteristic types of vibrational modes. In the low frequency range between ~400 and ~1600 cm^{-1}, the vibrations tend to be the result of single bond stretching modes, and bending modes in which the bond lengths remain the same but the angle between two bonds changes. The next frequency range falls between ~1500 and ~2500 cm^{-1} and is comprised of stretching modes of double bonds. Finally in the high frequency region above ~2800 cm^{-1} are the stretching modes between hydrogen and other heavier elements like carbon, oxygen and nitrogen.

Because the Raman spectrum depends on the structure and composition of a molecule, it can be a powerful tool in characterizing changes within a material. Each peak is associated with a specific bond, and therefore the

intensity of the peak is proportional to the concentration of that bond in the material. This information can be used to monitor the progress of chemical reactions. For example, in the case of a polymer undergoing crosslinking, the formation of each new crosslink will result in an increase in the peaks associated with the new bond. Likewise, as bonds are broken during a reaction, the intensity of the associated peaks will decrease.

Additionally, shifts in the wavenumber of a given peak indicate changes in the force constant of the corresponding bond. This behavior is analogous to the change in frequency of a plucked string as the tension on the string is increased or decreased. As a material is placed under tension or compression, the molecular bonds that are responsible for conveying the load will vibrate at a new frequency.[11, 13] Through carefully calibrated experiments, this behavior can be used as a molecular scale stress gauge that is intrinsic to the material. When combined with the correct optical setup, this can also be used to examine local residual stresses.

2.3 References

[1] B J.P.,Y S., *Molecular Hydrodynamics* (Dover Publications, New york, ed. 1, 1980).

[2] Masnik JE, Kieffer J,Bass JD. Structural Relaxations in Alkali Silicate Systems by Brillouin Light Scattering. Journal of the American Ceramic Society 1993;76(12):3073-80.

[3] Chung C-H,Yip S. Relaxation Equations for Depolarized Rayleigh and Brillouin Scattering in Liquids. Physical Review A Phys. Rev. A PRA 1971;4(3):928-39.

[4] Benassi P, Mazzacurati V, Ruocco G,Signorelli G. I - Elasto-optic constants in silicate glasses: Experiment and theory. Physical Review B Phys. Rev. B PRB 1993;48(9):5987-96.

[5] M Grimsditch, in *Brillouin Scattering*, Levy, Bass,Stern, Eds. (Academic press, 2001),

[6] JR Sandercock, in *Trends in Brillouin Scattering Studies of OpaqueMaterials, Supported Films, and CentralModes*, M Cardona,G Guntherodt, Eds. (Springer-Verlag, New York, 1982),

[7] Matusita K, Ihara C, Komatsu T,Yokota R. Photoelastic Effects in Phosphate Glasses. Journal of the American Ceramic Society 1985;68(7):389-91.

[8] Benassi P, Mazzacurati V, Monaco G, Ruocco G,Signorelli G. Brillouin and Raman cross sections in silicate glasses. Physical Review B Phys. Rev. B PRB 1995;52(2):976-81.

[9] Kato Y,Zdasiuk GA. Absolute measurements of Brillouin-scattering efficiencies of molecular liquids. J. Opt. Soc. Am. Journal of the Optical Society of America J. Opt. Soc. Am. 1975;65(9):995-8.

[10] k Nakomoto, *Infrared and Raman Spectra of Inorganic and Coordination Compounds part A: Theory and Applications in Inorganic Chemistry* (John Wiley & Sons Inc., Hoboken, NJ, ed. sixth, 2009).

[11] RM Silverstein, FX Webster,Dj Kiemle, *Spectrometric Identification of Organic Compounds* (John Wiley & Sons, Inc., Hoboken, NJ, ed. seventh, 2005).

[12] JW Robinson, EM Skelly Frame,GMII Frame, *Undergraduate Instrumental Analysis* (Marcel Dekker, New York, NY, ed. sixth, 2005).

[13] Young RJ. Monitoring Deformation Processes in High-performance Fibres using Raman Spectroscopy. Journal of the Textile Institute 1995;86(2):360-81.

Chapter 3

Cure Kinetics of DCPD

3.1 Introduction

Polymer matrix composites, due to their high strength and low density, are attractive material systems for improving vehicle efficiency in transportation applications. Fatigue cracks in these structures shorten the lifespan of components, and are difficult to detect and repair.[1] Self-healing polymer systems are being developed to remedy fatigue crack formation in composite structures. Dicyclopentadiene (DCPD) polymerized by Grubbs' catalyst has been used as such a system to heal cracks in thermoset polymer composites.[2, 3] To this end, microencapsulated liquid DCPD is dispersed throughout the polymer matrix, along with powdered Grubbs catalyst. When a crack cleaves a DCPD filled microcapsule, the liquid monomer discharges into the crack where it engulfs the catalyst particles exposed at the crack faces. [4, 5] Upon contact with DCPD, the catalyst initiates ring opening metathesis polymerization (ROMP) of the monomer, which then seals the crack with a highly cross-linked polymer network. The rate at which the network grows to span the crack dictates how effectively continued damage is prevented.[4, 6]

The DCPD monomer is composed of two parts: the norbornene ring and the cyclopentene ring shown in Figure 3.1(a). Each of these rings contains an unsaturated bond that acts as a reactive site for polymerization. The ruthenium-based Grubbs' catalyst engages the C=C double bonds and initiates ROMP at these sites.[7, 8] As the ring opens, the ruthenium-bearing moiety is transferred to one side of the opened bond, while the rest of the catalyst molecule attaches to the other side. The carbon double bond of the norbornene ring is under greater strain than the equivalent bond in the cyclopentene ring. This ring strain energetically favors opening of the norbornene ring over the cyclopentene ring during ROMP.[9, 10] Hence, during the initial stages of ROMP it is primarily the norbornene ring that participates in the polymerization, forming extended chains. Crosslinks between chains are formed with some delay, as the slower-reacting cyclopentene rings partake in the polymerization process. During polymerization, the ruthenium catalyst transfers to the most recently attached DCPD monomer, and consequently always remains at the end of the polymer chain.[11] This leaves it free to engage a new monomer and add it to the chain. Accordingly, the resulting polymer structure delineates the trajectory of catalyst units, and the final network topology strongly depends on the ability of the catalyst to reach new monomers or unreacted network segments.

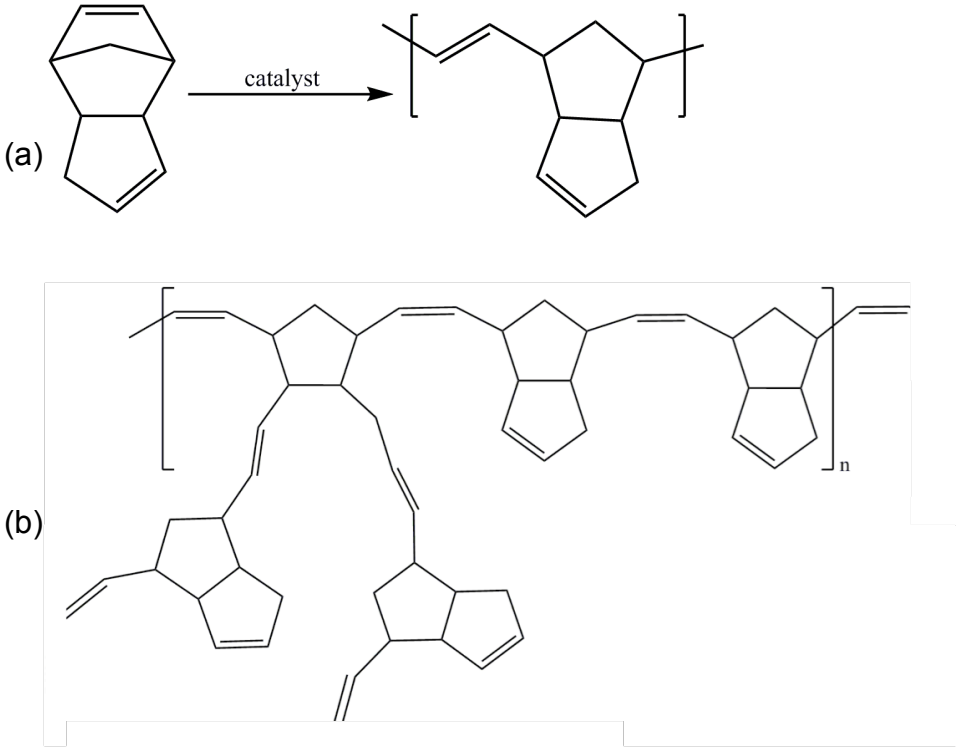

Figure 3.1 Schematic of DCPD and ROMP

We have used concurrent Raman and Brillouin light scattering methods to monitor the curing behavior of DCPD during ROMP in order to construct a kinetic model of the cure reaction, and to predict the mechanical properties of the resultant DCPD network formed. Because Raman scattering is sensitive to chemical bond configurations, we can use it to track the behavior of specific reactive sites on the monomer, thus providing us with a more detailed description of the cure behavior than could be achieved using calorimetric cure measurements. Using the Raman derived results as a guide, we have developed a detailed kinetic model that reproduces the cure behavior of DCPD undergoing ROMP. While Raman light scattering measurements provide insight as to the state of cure of the system, Brillouin scattering measurements yield information about the rigidity, and hence, the structural integrity of the DCPD network.

Brillouin scattering has been demonstrated to be an effective tool to monitor in-situ changes in the elastic properties of polymers during cure.[12-14] It is a well-suited technique for this purpose, because it yields elastic properties of a sample without mechanically disturbing the system being probed. By comparing the two complementary datasets, we can link the elastic behavior of the network to the reaction kinetics that drive network formation. This work is an expansion of our prior efforts in characterizing this system.[15] The revised reaction model considers the catalyst attachment point in the kinetic cure model, and also examines the development of network stiffness as a function of the cure reaction.

3.2 Experimental Methods

A series of DCPD samples were prepared with different concentrations of first generation Grubbs' catalyst. In order to ensure optimal performance, the catalyst was first dissolved in benzene, and freeze-dried. This process reduces the size of catalyst particles, which improves the dissolution rate of the catalyst in liquid DCPD.[16, 17] The DCPD samples were prepared using four different catalyst concentrations: 0.50, 0.45, 0.40 and 0.35 wt%. Using higher concentrations resulted in samples that cured at such a high rate that we were unable to collect sufficient Raman and Brillouin spectra for useful analyses. Samples mixed with catalyst concentrations below 0.35 wt% produced erratic cure behavior, often failing to fully harden. The desired amount of catalyst was weighed and added to a glass vial for each sample. In order to break up any clumps of catalyst particles, each vial containing powdered catalyst was immersed in a sonication bath and sonicated for one minute. Next, 2 ml of DCPD

were mixed with the powdered catalyst. Each mixture of DCPD and catalyst was sonicated for an additional minute in order to mix the catalyst uniformly with the DCPD and to further break up any remaining clumps of catalyst particles. Finally, each sample was injected into a sample holder and placed in the optical path of a 532 nm Coherent Verdi laser. A nominal laser output power of 80 mW was used for all measurements.

We collect the scattered light using platelet geometry, in which the sample is sandwiched between two parallel windows, and the plane of the windows bisects the angle formed by the incident and the scattered light. This geometry has been developed for Brillouin scattering to cancel out any effects of the index of refraction on the observed frequency shift in the Brillouin spectrum.[18] The scattered light from the sample is collected using a 150 mm collimating lens. The focal volume for this setup is about 50 μm in diameter. A set of moveable mirrors is used to direct the collimated light to each of our spectrometers.

Our Raman spectra are measured using a Princeton Instruments TriVista triple monochrometer fitted with a Spec 10 liquid nitrogen cooled CCD detector. Raman spectra are centered at 1600 cm^{-1} in order to observe the peaks corresponding to C=C stretching modes in the DCPD monomer. Each Raman spectrum is collected for one minute. Our Brillouin spectra are collected using a Sandercock six-pass tandem Fabry-Perot interferometer. Brillouin spectra are collected for about three minutes using 512 binning channels in order to improve the collection time.

In order to assign the experimentally observed Raman peaks, we used density functional theory (DFT) calculations to determine the vibrational modes of specific molecular structures formed as a results of the curing process in DCPD. Further calculations were performed to predict the respective enthalpies of the two reactive sites on the DCPD monomer. The molecular structure of each configuration was optimized in the Cartesian coordinate systems without symmetry constraints in Gaussian 03 [19], using the B3LYP exchange correlation functional [20] and the 6-31G* contracted basis set with polarization functions.[21, 22]

The Raman spectra cover the spectral range from 1440 to 1750 cm^{-1}. In this region of the Raman spectra, seven peaks are observed over the course of the curing process as shown in Figure 3.2. The vibrational modes associated with these peaks are determined using DFT calculations and crosschecked against available experimentally determined mode assignments.[10, 23] The two peaks at 1445 and 1455 cm^{-1} are associated with C-H bending modes. The concentration of these bonds is unaffected by the cure reaction and as such, remains constant throughout all measurements. We observe three peaks associated with stretching modes of the C=C bonded reactive sites. The 1575 cm^{-1} peak is attributed to stretching of the C=C bond in the norbornene ring. During ROMP, the norbornene rings are opened, eliminating this bond geometry. As a result, the intensity of the 1575 cm^{-1} peak decreases proportionally. The two peaks at 1619 and 1625 cm^{-1} are attributed to the C=C stretching mode of the cyclopentene ring. In unreacted DCPD, only the 1619 cm^{-1} peak is present. As

the norbornene opens, ring strain in the cyclopentene portion of the monomer is relaxed, which results in a shift of the 1619 cm^{-1} mode to 1625 cm^{-1}. Therefore, the intensity of the 1619 cm^{-1} peak decreases as the norbornene rings are opened, while the 1625 cm^{-1} peak grows. Our experimental spectra agree with this prediction from the DFT calculations, showing that the 1575 and 1619 cm^{-1} peak intensities decrease at the same rate over the course of the curing process. Finally, the 1655 and 1666 cm^{-1} peaks do not appear until the cure process begins. They form as a result of the cure and are attributed to C=C stretch modes in the developing polymer chains. Specifically, the 1655 cm^{-1} peak is associated with *cis*-conformed C=C bonds while the 1666 cm^{-1} peak is associated with *trans*-conformed bonds. A summary of the Raman mode assignments is given in Table 3.1.

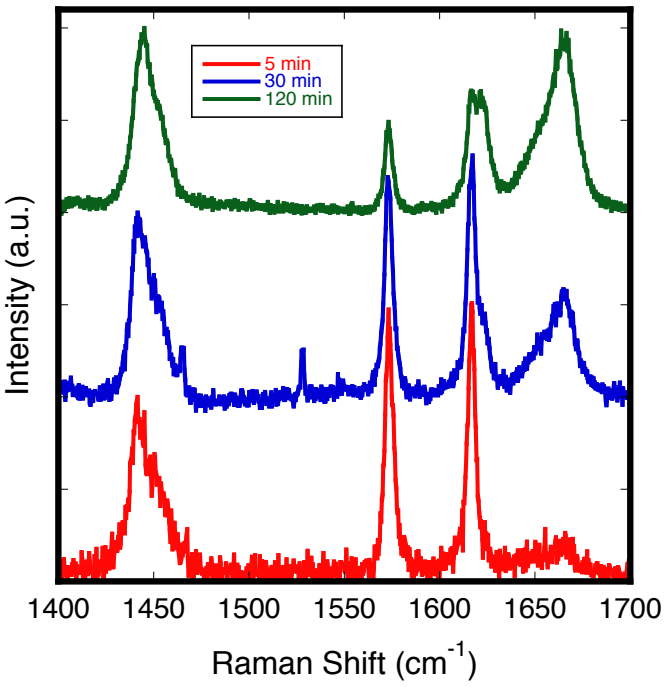

Figure 3.2 Raman spectra of DCPD at three times during the curing process

Raman Mode Assignment	Raman Shift (cm^{-1})
C-H bending	1445
C-H bending	1455
Norbornene C=C stretch	1575
Cyclopentene C=C stretch (norbornene ring intact)	1619
Cyclopentene C=C stretch (norbornene ring open)	1625
Cis-conformed C=C stretch	1655
Trans-conformed C=C stretch	1666

Table 3.1 Raman mode assignments for DCPD

Brillouin scattering measures the Doppler shifted frequency of light scattered by propagating thermal phonons in a sample medium. This yields mechanical information from the sample without interfering with the formation of the polymer network. It is possible to observe scattering for both longitudinal and shear phonons using Brillouin scattering. However, the intensity of scattering from shear phonons is much weaker, and in the case of DCPD, we do not observe peaks related to shear waves. The wave vector, *q*, of the scattering phonon is the difference between the incident and scattered light wave vectors as required by wave vector conservation rules.[24] From this information we can calculate the velocity of sound in the sample according to: $c_L = \frac{\Delta\omega_B}{|q|}$, where $\Delta\omega_B$ is the measured frequency shift of the scattered light from the incident light frequency. For platelet geometry the magnitude of the wave vector is given by $|q| = 2sin(\theta)/\lambda_0$.[18] Here θ is the angle between the incident light, and a vector normal to the sample plane, and λ_0 is the wavelength of the incident light. Using both the measured phonon velocity and the sample density, ρ, we can calculate the adiabatic longitudinal elastic modulus according to

$$M' = \rho c_L^2 = \frac{E(1-\nu)}{(1+\nu)(1-2\nu)} \tag{3.1}$$

where E is the Young's modulus, and ν is the Poisson's ratio.

3.3 DCPD Reaction Kinetics

In order to model the reaction of DCPD, we initially consider all of the possible species that could form or be consumed during ROMP process. First, we note that there are two reactive sites that can undergo ROMP: the C=C bonds in the norbornene and cyclopentene rings. It has been shown that the norbornene ring is energetically favored to open first because the corresponding double bond is under greater strain than the equivalent double bond in the cyclopentene ring. [10] Isothermal DSC investigations of DCPD cured by ROMP show that the glass transition temperature as a function of cure is independent of the reaction temperature. This behavior implies that the norbornene and cyclopentene rings open sequentially. [25] Therefore, in our model, we use the assumption that the norbornene ring will always open first. Secondly, we assume that a reactive site will undergo ROMP only when it reacts with a catalyst molecule. The catalyst can exist freely in solution or attached to a monomer unit after an initial ROMP reaction. Because there are two possible reactive sites on the DCPD monomer, there can be up to two catalyst moieties attached to a given monomer unit. We therefore define the species present in the reaction as Q_{ij}, where i enumerates the number of sites on the monomer that have undergone ROMP, and j enumerates the number of attached catalyst moieties. Assuming the norbornene ring always opens first, Q_{1j} always refers to a monomer unit with

the cyclopentene ring intact. Finally, the species C denotes the free catalyst molecules in the solution. These species may all react with one another at different rates to form the DCPD network, as described in Table 3.2.

Reaction description	Rate of reaction
$Q_{00} + C \overset{k_1}{\Rightarrow} Q_{11}$	$r_1 = k_1[Q_{00}][C]$
$Q_{00} + Q_{11} \overset{k_2}{\Rightarrow} Q_{11} + Q_{10}$	$r_2 = k_2[Q_{00}][Q_{11}]$
$Q_{00} + Q_{21} \overset{k_3}{\Rightarrow} Q_{11} + Q_{20}$	$r_3 = k_3[Q_{00}][Q_{21}]$
$Q_{00} + Q_{22} \overset{k_4}{\Rightarrow} Q_{11} + Q_{21}$	$r_4 = k_4[Q_{00}][Q_{22}]$
$Q_{10} + C \overset{k_5}{\Rightarrow} Q_{21}$	$r_5 = k_5[Q_{10}][C]$
$Q_{10} + Q_{11} \overset{k_6}{\Rightarrow} Q_{21} + Q_{10}$	$r_6 = k_6[Q_{10}][Q_{11}]$
$Q_{10} + Q_{21} \overset{k_7}{\Rightarrow} Q_{21} + Q_{20}$	$r_7 = k_7[Q_{10}][Q_{21}]$
$Q_{10} + Q_{22} \overset{k_8}{\Rightarrow} Q_{21} + Q_{21}$	$r_8 = k_8[Q_{10}][Q_{22}]$
$Q_{11} + C \overset{k_9}{\Rightarrow} Q_{22}$	$r_9 = k_9[Q_{11}][C]$
$Q_{11} + Q_{11} \overset{k_{10}}{\Rightarrow} Q_{22} + Q_{10}$	$r_{10} = k_{10}[Q_{11}][Q_{11}]$
$Q_{11} + Q_{21} \overset{k_{11}}{\Rightarrow} Q_{22} + Q_{20}$	$r_{11} = k_{11}[Q_{11}][Q_{21}]$
$Q_{11} + Q_{22} \overset{k_{12}}{\Rightarrow} Q_{22} + Q_{21}$	$r_{12} = k_{12}[Q_{11}][Q_{22}]$

Table 3.2 Possible reactions within the DCPD system

The brackets around the species symbols denote the molar concentration of each species. The reaction rates k_i are assumed to be temperature dependent according to a standard Arrhenius form: $k_i = A_i e^{-\frac{Ea_i}{RT}}$. Here A_i is a rate constant, and Ea_i is the activation energy of the reaction *i*. These reaction rates can be combined to describe the rates of formation of each reactive species as follows:

$$[\dot{C}] = -(r_1 + r_5 + r_9) \tag{3.2}$$

$$[\dot{Q_{00}}] = -(r_1 + r_2 + r_3 + r_4) \tag{3.3}$$

(3.5) $$[\dot{Q_{10}}] = (r_2 + r_6 + r_{10}) - (r_5 + r_6 + r_7 + r_8)$$

(3.6) $$[\dot{Q_{21}}] = (r_4 + r_5 + r_6 + r_7 + 2r_8 + r_{12}) - (r_3 + r_7 + r_{11})$$

(3.7) $$[\dot{Q_{22}}] = (r_9 + r_{10} + r_{11} + r_{12}) - (r_4 + r_8 + r_{12})$$

(3.8) $$[\dot{Q_{20}}] = (r_3 + r_7 + r_{11})$$

Because the ROMP of DCPD is exothermic and the reaction rates are temperature dependent, we also include the following equation to describe the changes in temperature as a function of cure:

(3.9) $$\dot{T} = \frac{1}{mc_p}\left(-hA(T - T_a) + \sum_i (r_i \Delta H_i)\right)$$

Here m is the sample mass, c_p is the heat capacity, h is the heat transfer coefficient between the sample container and air, A is the surface are of the sample, T_a is the ambient temperature for the experiment, and ΔH_i is the enthalpy of the reaction denoted by its subscript.

Together, these equations describe all of the possible chemical interactions between the catalyst and the monomer, including the positions on the monomer units where the catalyst is attached. However, given that each reaction rate, $r_{i,}$ contains two constants, this system contains seven equations with 22 unknowns, making it impractical to solve numerically. In order to condense these equations into a more manageable package, we must take into

account the information contained in our chemical probe, namely the Raman spectrum of the reacting DCPD system.

As previously discussed, the Raman spectrum of DCPD contains three peaks associated with stretching of the C=C bonded reactive sites. The 1575 cm^{-1} peak is attributed to C=C stretching in the norbornene ring. During ROMP, the concentration of norbornene rings decreases. As a result of this, the intensity of the 1575 cm^{-1} peak decreases proportionally. The two peaks at 1619 and 1625 cm^{-1} are attributed to the C=C stretching mode of the cyclopentene ring. Initially only the 1619 cm^{-1} peak is present, but as the norbornene ring opens, it relaxes the strain in the cyclopentene portion of the monomer, which causes the 1619 cm^{-1} mode to shift to1625 cm^{-1}. Therefore, as the number of norbornene rings decreases, so too does the intensity of the 1619 cm^{-1} peak, while the 1625 cm^{-1} peak grows. Together these peaks give us enough information to calculate the concentration of each DCPD reactive site in our system. The Raman spectrum does not, however, let us determine where on the monomer the catalyst may be attached. Using the observable Raman modes as a guide, an alternate set of reactive species can be defined that only takes into account experimentally observable quantities:

$$[\Phi_0] = [Q_{00}] \tag{3.10}$$

$$[\Phi_1] = \sum_j [Q_{1j}] \tag{3.11}$$

$$[\Phi_2] = \sum_j [Q_{2j}] \tag{3.12}$$

$$[\mathrm{C}_R] = C + [Q_{11}] + [Q_{21}] + 2[Q_{22}]. \tag{3.13}$$

Experimentally these concentrations can be calculated based on the intensities of the 1575, 1619, and 1625 cm^{-1} Raman peaks according to:

$$[\Phi_0] = \frac{I_{1575}}{I^0_{1575}} \tag{3.14}$$

$$[\Phi_1] = \frac{I_{1625}}{I^0_{1619}} \tag{3.15}$$

$$[\Phi_2] = 1 - [\Phi_0] - [\Phi_1]. \tag{3.16}$$

Here I^0 and I are the Raman peak intensities of the designated peak for the start of the reaction and for any point thereafter, respectively. Furthermore, we can calculate the degree of cure, defined as the fraction of reactive sites that have undergone ROMP, from the species concentrations as follows:

$$\alpha = 1 - [\Phi_0] - \frac{[\Phi_1]}{2}. \tag{3.17}$$

Using these equations, we can therefore determine the time dependence of the cure process. The symbols in Figure 3.3 (a) represent the experimentally measured degree of cure vs time for all four catalyst concentrations tested, while the symbols in Figure 3.3 (b) represent the species concentrations and degree of cure as a function of time for the system with 0.4 wt% catalyst concentration.

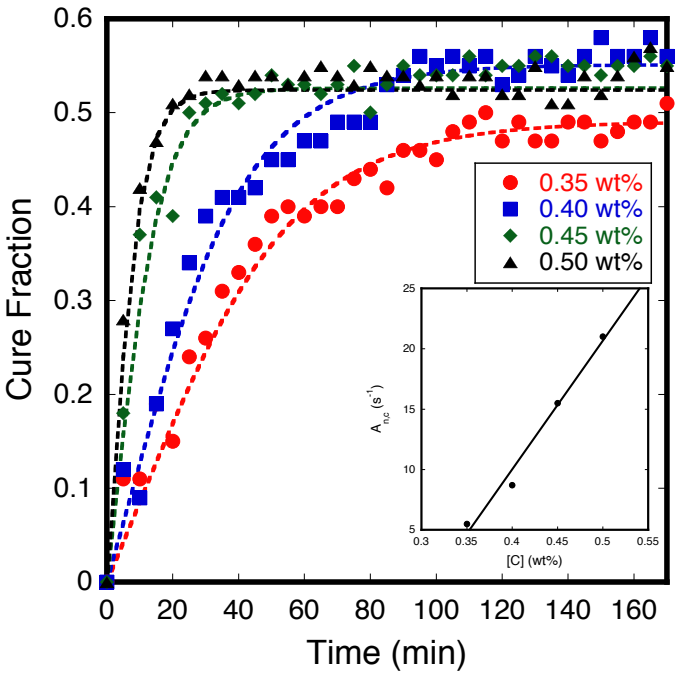

(a)

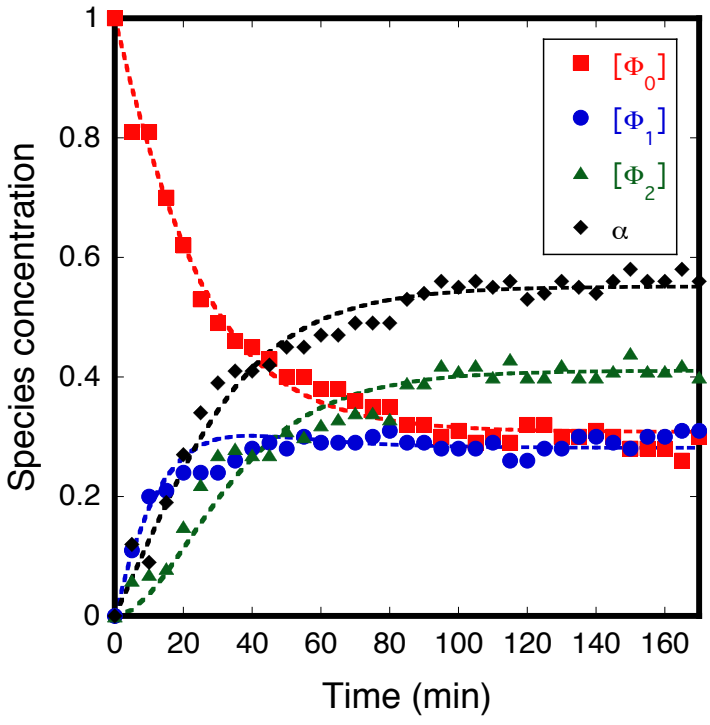

(b)

Figure 3.3 (a) DCPD degree of cure as a function of time. Inset: rate constants as a function of catalyst loading. (b) Species concentrations as a function of time for 0.4 wt% catalyst concentration

Because the experimentally observable reactive species do not contain information about the catalyst location, the rate equations that describe their concentrations should also be independent of catalyst position. To develop these equations, we define: $k_1 = k_3 = k_3 = k_4 = k_N$, and $k_5 = k_6 = \ldots = k_{12} = k_C$. We also assume that the enthalpy of reaction for norbornene and cyclopentene each remain unaffected by the location of the catalyst, i.e. $\Delta H_1 = \Delta H_2 = \Delta H_3 = \Delta H_4 = \Delta H_N$, and $\Delta H_5 = \Delta H_6 = \ldots = \Delta H_{12} = \Delta H_C$. These simplifications yield a condensed set of rate equations:

$$[\dot{\Phi}_0] = -K_N[\Phi_0][\mathrm{C}_R], \tag{3.18}$$

$$[\dot{\Phi}_1] = K_N[\Phi_0][\mathrm{C}_R] - K_C[\Phi_1][\mathrm{C}_R], \tag{3.19}$$

$$[\dot{\Phi}_2] = K_C[\Phi_1][\mathrm{C}_R], \tag{3.20}$$

$$[\dot{\mathrm{C}_R}] = 0, \tag{3.21}$$

$$\dot{T} = \frac{1}{mc_p}\left(-hA(T - T_a) + K_N \Delta H_N [Q_0][C_R] + K_C \Delta H_C [Q_1][C_R]\right). \tag{3.22}$$

The Raman spectra show that the peaks at 1575, 1619, and 1625 cm^{-1} do not completely disappear at the end of the curing process. This demonstrates significant reactive site functionality remains at the end of the cure process as is observed in Figure 3.3 (b). This occurs because the mobility of the catalyst is reduced as the network density increases. At some point, the catalyst mobility decreases to the point where it can no longer access the remaining reactive sites, and ROMP stops. We take this development into account by gradually

lowering the concentration of active catalyst with increasing degree of cure according to

$$[\dot{C_R}] = -K_S[C_R]([\Phi_1] + [\Phi_2])^2 \quad (3.23)$$

While this is a strictly empirical expression, it adequately models the premature end of cure that we observe experimentally. This equation takes into account the proportion of DCPD monomer incorporated into the network ($[\Phi_1] + [\Phi_2]$), so that as the network grows, the catalyst availability becomes increasingly limited.

In our experiments, the sample mass *m* is 0.831g, and the heat capacity c_p is 1.112 J/gK. The heat transfer term *hA* is 0.02J/K. The ambient temperature for the experiments is 295 K. We obtained values for the enthalpies of reaction from DFT calculations.[15] The ground state energies of each species are compared to one another to find the total change in energy for each reaction. This method yields –140.85 kJ/mol and –38.59 kJ/mol as the values of ΔH_1 and ΔH_2 respectively. The system of reaction equations for the experimentally observable species was numerically fitted to the measured species concentrations using a least squares fitting method. To further reduce the number of free variables to be solved, we fixed the rate constant elements A_N and A_C of the reaction rates to be equal. This is a reasonable assumption, because the geometry and frequency of interaction between the catalyst molecules and norbornene and cyclopentene sites should be similar. A difference in reaction rates between the two sites is accounted for as a result of their activation energies being different.[10, 26] As a result of our assumptions, the

remaining fitting parameters for the reacting DCPD system are Ea_N, Ea_C, A_N, and K_S. In Figure 3.3 (a) we compare the degree of cure as a function of time predicted by the model with the data derived from the analysis of the Raman spectra for all catalyst concentrations. Figure 3.3 (b) compares the modeled species concentrations to the experimentally determined values for the system containing 0.4 wt% catalyst. The best-fit values for these parameters are summarized in Table 3. While the activation energies appear to be independent of the catalyst concentration, the rate constants depend linearly on it, as shown in the inset of Figure 3.3 (a). The equation for the line describing this dependence is $A_N = A_C = -32.6 + 106.5[\mathrm{C}_R]$. This equation suggests that a minimum catalyst loading of about 0.3 wt% is required to drive the ROMP reaction. This threshold likely explains the erratic curing behavior that we observed for samples with catalyst concentrations below 0.35 wt%. Furthermore this linear dependence means that for concentrations above the 0.3 wt% threshold, the rate equations for $[\Phi_0]$, $[\Phi_1]$, and $[\Phi_2]$ are dependent on the square of the catalyst concentration. This suggests that there may be a more complex interaction between the catalyst and the monomer during ROMP than has been generally assumed. However, the information in this dataset cannot help us identify precisely how this interaction may work.

Parameter	0.35 wt%	0.40 wt%	0.45 wt%	0.50 wt%
Ea_N (J/mol)	5995	6497	5979	6001
Ea_C (J/mol)	5494	5953	5478	5499
A_N, A_C (s^{-1})	5.5	8.7	15.5	21.0
K_S	0.00140	0.00144	0.00426	0.00661

Table 3.3 Best Fit parameters for DCPD cure reaction

It is also worth noting that the rate coefficient for the reaction of the norbornene (Kn) is about 19% lower than for the cyclopentene rings (Kc). This is unexpected because the norbornene is known to react before the cyclopentene ring. We believe that the opening of the norbornene ring during ROMP affects the reactivity of the cyclopentene ring, causing it to increase. The Raman mode of the cyclopentene reactive site at 1619 cm^{-1} moves to a higher energy at 1625 cm^{-1} during the reaction. This increased vibrational energy could serve to lower the activation barrier towards reaction, and could explain the observed higher reaction rate for the cyclopentene ring.

3.4 Elastic modulus

We measured the longitudinal elastic modulus of the curing DCPD concurrently with the degree of cure data as described in the Methods section. These measurements allow us to analyze the modulus as a function of time and degree of cure during polymerization. Figure 3.4 shows the measured modulus as a function of time. This plot is similar to the cure as a function of time, given that as the Grubbs's catalyst concentration is increased, the rate of reaction increases proportionally, and that the modulus asymptotically approaches its final value. However the initial and final elastic moduli of the system also show a dependence on the catalyst concentration, namely increasing linearly with the catalyst concentration as shown in Figure 3.4 (inset).

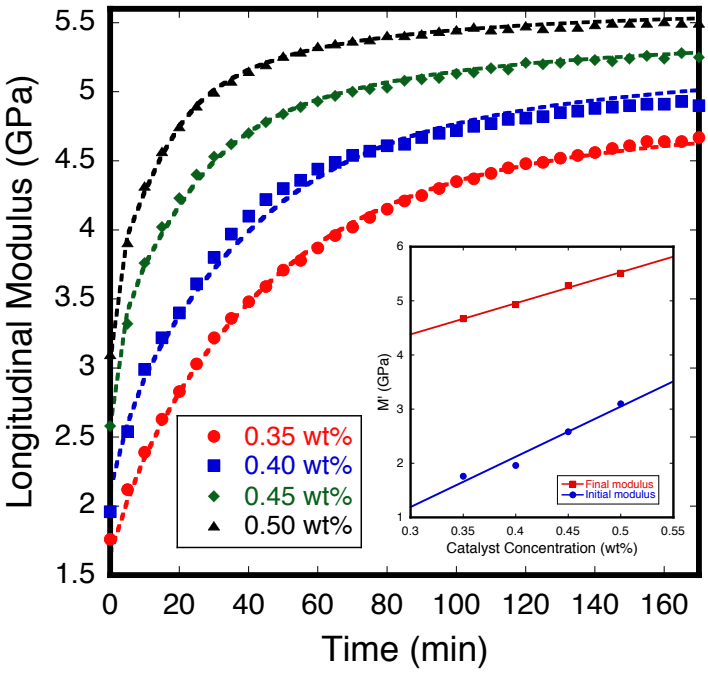

Figure 3.4 Longitudinal elastic modulus as a function of time Inset: initial and final moduli as a function of catalyst concentration

The most striking feature of the evolution of the elastic modulus, however, only becomes apparent when it is plotted as a function of cure as in Figure 3.5. Here we see that once the maximum cure has been reached at slightly past 50% conversion, the modulus continues to increase. This effect is most significant for the higher catalyst concentrations, for which the increase in modulus is roughly 0.5 GPa, whereas the 0.35 wt% system only shows a minimal effect. It is likely that during polymerization the initial structure imposed on the network by the cure process does not correspond to a local energy minimum. For example, Van der Waals forces between network units may be maximized for specific orientations that differ from those imposed by the cure process. Over time the network may

then relax to a more stable configuration over a longer time scale than the cure reaction.

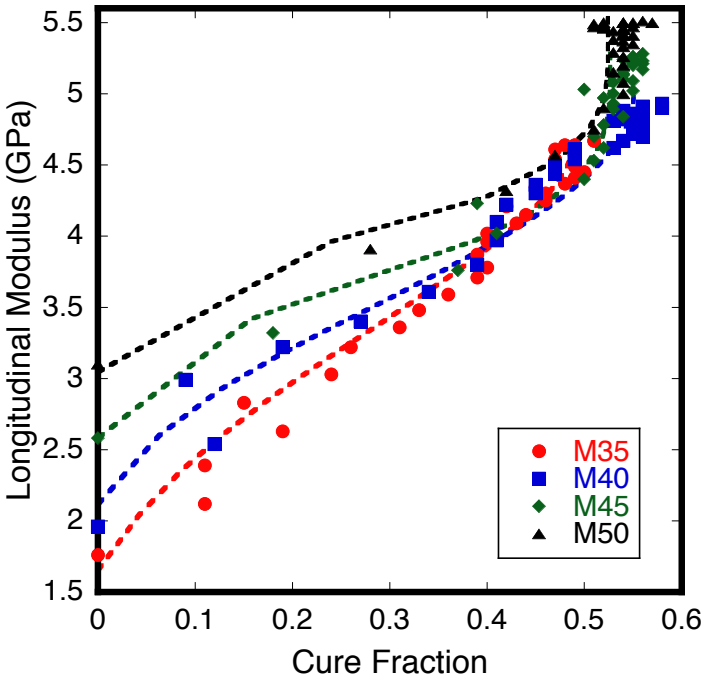

Figure 3.5 Elastic modulus as a function of degree of cure

To explain this behavior we developed a model describing the time evolution of the longitudinal elastic modulus of DCPD. This model must account for the reaction kinetics, as the formation of the permanent bonds can be expected to enhance the stiffness of the network. However as the final increase of the modulus at constant degree of cure revealed in Figure 3.5 suggests, the model must also take into account stiffening of the DCPD network by mechanisms other than new covalent bond formation. To relate the modulus to the various network components, we treat the curing system as a composite of homogenously mixed components, which are the same reactive species defined previously for the reaction model. Because each of our components is composed

of the same atoms, under different configurations, we assume that their specific volumes are similar, and accordingly weigh their contributions to the total elastic modulus by their molar concentrations. The total elastic modulus then is the sum of the contributions from each component i.e.:

$$M'([\Phi_0],[\Phi_1],[\Phi_2]) = M'([\Phi_0]) + M'([\Phi_1]) + M'([\Phi_2]). \quad (3.24)$$

Up to the time when the catalyst is added to the DCPD, no network formation has occurred, and the only contributions to the elastic modulus are the catalyst molecules, and the Φ_0 monomer species. We can therefore use the linear fit from Figure 3.4 to define the Φ_0 contribution to the elastic modulus as:

$$M'([\Phi_0]) = (-1.594 + 928[C_R])[\Phi_0] \quad (3.25)$$

The contributions of Φ_1 and Φ_2 are not obvious from the data comparing the modulus to the degree of cure. A first approximation would be to simply weigh their contributions to the final modulus linearly with respect to their concentrations as follows:

$$M'([\Phi_1],[\Phi_2]) = A[\Phi_1] + B[\Phi_2] \quad (3.26)$$

This approximation lacks any non-covalent contributions to the modulus, and results in the best-fit curves shown in Figure 3.6. Accordingly, there are some fundamental discrepancies between the experimental data and the model of eq. 3.26. In particular, the measured modulus continues to increase well after changes in the reactive species concentrations have stopped. In fact, for the

highest catalyst loading, the modulus increases for nearly two hours after the cure reaction has ended.

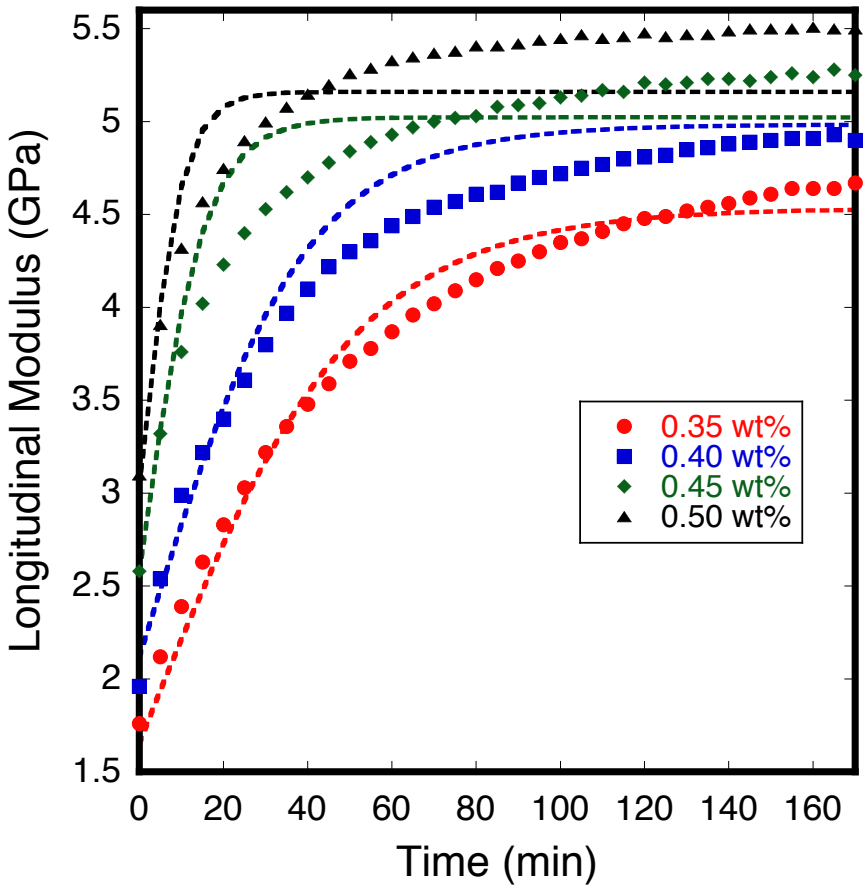

Figure 3.6 The experimentally observed elastic modulus is poorly fit as a simple linear combination of the reactive species concentrations

In order to address this observed difference in the modulus and cure time scales, we introduce a term to the Φ_1 and Φ_2 contributions to the elastic modulus that accounts for network relaxation without change in the bonding pattern. Not knowing details about the relaxation mechanism, we allow for multiple intermediate relaxation steps that cumulatively contribute to the total degree of relaxation of the DCPD system. As an illustration, Figure 3.7 shows the

difference in the relaxation behavior for three model systems with different numbers of intermediate relaxation states. With increasing number of consecutive relaxation steps, the curves exhibit a more pronounced inflection, reflecting an initial delay and subsequent acceleration in the relaxation behavior. Therefore, a generalized term that can account for multiple relaxation steps should be sigmoidal in shape. It is not practical to find a closed form solution for a relaxation term that can accommodate an unknown number of relaxations. Instead we use a simplified sigmoidal function that approximates this behavior. After investigating a series of common functional forms, we found that using a stretched exponential function to model the relaxation behavior works best. We also found that, when modifying both the ϕ_1 and ϕ_2 terms with such a stretched exponential, the role of the ϕ_1 term is relatively inconsequential compared to the ϕ_2 term, i.e., linear chains relax much faster than the cross-linked network segments. Hence, for the sake of simplicity, our revised model is

$$M'([\Phi_1],[\Phi_2],t) = A[\Phi_1] + B[\Phi_2]e^{-\left(H/t\right)^{\beta}} \tag{3.27}$$

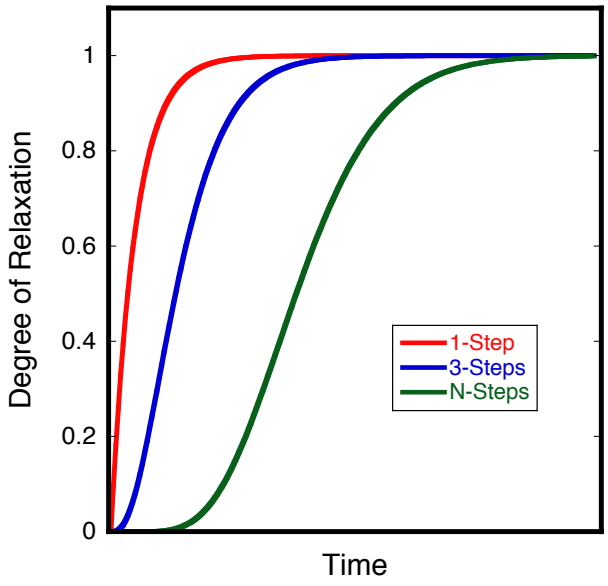

Figure 3.7 Relaxation behavior for systems with increasing numbers of intermediate relaxation steps

Best fits of the data using eq. (27) are shown in Figs. (3.4) and (3.6). The values for *A* and *B* are the same within their error, namely 6.85 ±0.21 GPa and 6.79 ±0.11 GPa, respectively. These results suggest that the incorporation of the monomer unit into the network contributes more to the final value of the modulus than the number of bonds by which each element is connected to the network. The time dependent term increases the influence of the Φ_2 species as time increases, so that once the cure reaction has ended, the total modulus will continue to asymptotically approach its maximum value. In a stretched exponential, the stretching parameter of the exponential, β, is constrained between zero and one. For our system we found β to be 0.913 ±0.12. The term *H* controls the rate of this process such that for a larger value of *H*, it takes longer for the modulus to reach an equilibrium value. As can be seen in Figure 8, *H* changes linearly with catalyst concentration so that a system that cures at a

faster rate, also reaches equilibrium faster. However, the increase in relaxation rate lags behind the increase in cross-link rate. The fact that the rate-limiting mechanism in this structural relaxation is associated with the Φ_2 term supports the idea that this phenomenon is a form of structural relaxation. The crosslinked components of the network are more constrained in their movement than the linearly bonded components. As a result, the crosslinks impede relaxation into a preferred structural configuration, resulting in a delay in the development of the elastic modulus. The sigmoidal shape of the time dependent component suggests an accelerating nature of this relaxation process. It is possible that once a certain number of network units have reached a relaxed state, the constraints on relaxation for the rest of the cross-linked units are reduced, and the relaxation process proceeds more quickly.

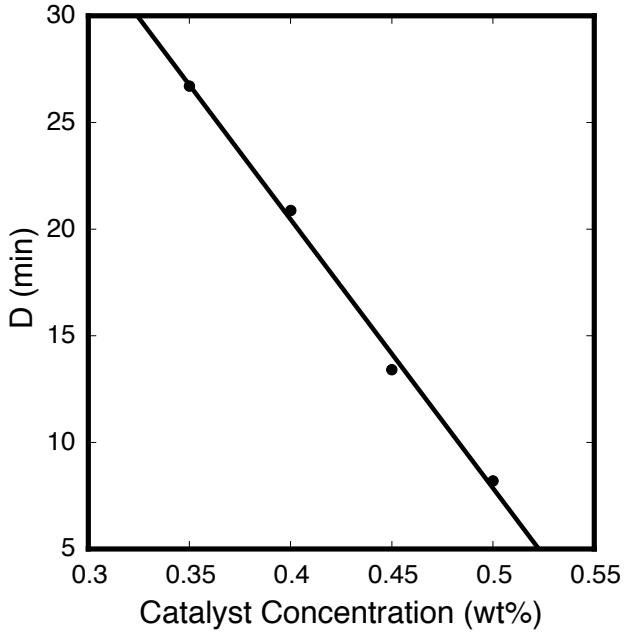

Figure 3.8 Coefficient H as a function of catalyst concentration

3.5 Conclusion

We have used concurrent Raman and Brillouin light scattering techniques to monitor the *in situ* change in elastic properties as well as the chemical configuration of DCPD during ROMP. Combining these methods has allowed us to construct a model of the cure kinetics of DCPD, as well as a model of how the elastic properties depend on the underlying chemical reactions taking place. The kinetic reaction model shows that the reaction rate of the DCPD depends on the square of the catalyst concentration, and that there is a minimum threshold for the catalyst concentration below which the reaction will not occur. It also shows that the reaction rates for the cyclopentene and norbornene sites are similar, with the cyclopentene appearing to react more quickly. We believe that this occurs because the opening of the norbornene ring lowers the activation barrier for the cyclopentene ring reaction. This mechanism is suggested by the observed frequency shift in the Raman mode associated with the cyclopentene reactive site. The elastic modulus data show that once the cure reaction has ended, the DCPD network continues to stiffen by a significant amount. The specific mechanism for this behavior is unclear: however, it seems that the network structure undergoes a multistep relaxation process before reaching an equilibrium state. This process appears to be governed by the crosslinking species, likely because the crosslinks impose greater constraints on the mobility of network elements. The elastic modulus of the network can be modeled by a linear combination of the reactive species concentrations. Interestingly, Φ_1 and

Φ_2 both seem to contribute an equal amount to the final elastic modulus of the network.

3.6 References

[1] Gamstedt EK,Talreja R. Fatigue damage mechanisms in unidirectional carbon-fibre-reinforced plastics. Journal of Materials Science 1999;Journal of Materials Science 34(11):2535-46.

[2] White SR *et al.* Autonomic healing of polymer composites. Nature 2002;409(794-817.

[3] White SR, Caruso MM,Moore JS. Autonomic Healing of Polymers. MRS BULLETIN 2008;33(766-9.

[4] Brown E, White S,Sottos N. Retardation and repair of fatigue cracks in a microcapsule toughened epoxy composite—Part II: In situ self-healing. Composites Science and Technology 2005;65(15-16):2474-80.

[5] Brown E, White S,Sottos N. Fatigue crack propagation in microcapsule-toughened epoxy. Journal of Materials Science 2006;41(19):6266-73.

[6] Jones A, Rule J, Moore J, Sottos N,White S. Life extension of self-healing polymers with rapidly growing fatigue cracks. J R Soc Interface 2007;4(13):395-403.

[7] Kessler M, Larin G,Bernklau N. Cure characterization and viscosity development of ring-opening metathesis polymerized resins. Journal of Thermal Analysis and Calorimetry 2006;85(1):7-12.

[8] Kessler M,White S. Cure kinetics of the ring-opening metathesis polymerization of dicyclopentadiene. JOURNAL OF POLYMER SCIENCE PART A POLYMER CHEMISTRY 2002;40(14):2373-83.

[9] Della M, A., Hilborn JG,Mã¼Hlebach A. Macroporous Cross-Linked Poly(dicyclopentadiene). Macromolecules 2000;33(8):2916-21.

[10] Schaubroeck D, Brughmans S, Vercaemst C, Schaubroeck J,Verpoort F. Qualitative FT-Raman investigation of the ring opening metathesis polymerization of dicyclopentadiene. Journal of Molecular Catalysis. A, Chemical 2006;254(1-2):180-5.

[11] Maiti S, Shankar C, Geubelle P,Kieffer J. Continuum and Molecular-Level Modeling of Fatigue Crack Retardation in Self-Healing Polymers. Journal of Engineering Materials and Technology 2006;128(595.

[12] Fioretto D *et al.* Cauchy relation in relaxing liquids. J Chem Phys 2008;128(21):214502.

[13] Kruger J *et al.* Cauchy-like relation between elastic constants in amorphous materials. Physical Review B 2002;66(1):12206.

[14] Müller U *et al.* Acoustic profilometry of interphases in epoxy due to segregation and diffusion using Brillouin microscopy. New Journal of Physics 2008;10(2):023031.

[15] Aldridge M *et al.* Combined Experimental and Simulation Study of the Cure Kinetics of DCPD. Journal of Composite Materials 2010;44(22):2605-18.

[16] Jones AS, Rule JD, Moore JS, White SR,Sottos NR. Catalyst Morphology and Dissolution Kinetics of Self-Healing Polymers. Chemistry of Materials Chemistry of Materials Chem. Mater. 2006;18(5):1312-7.

[17] Wilson GO, Caruso MM, Reimer NT, Sottos NR,White SR. Evaluation of Ruthenium Catalysts for Ring-Opening Metathesis Polymerization-Based Self-Healing. Chem. Mater 2008;20(3288-97.

[18] Kruger J, Peetz L,Pietralla M. Brillouin scattering of semicrystalline poly(4-methyl-1-pentene): study of surface effects of bulk and film material. Polymer 1978;19(12):1397-404.

[19] Frisch MJ *et al.* Gaussian 03, Revision C.02. Gaussian 03, Revision C.02 2004;

[20] Becke A. Density-functional thermochemistry. III. The role of exact exchange. Journal of Chemical Physics 1993;98(7):5648-52.

[21] Francl MM *et al.* Self-consistent molecular orbital methods. XXIII. A polarization-type basis set for second-row elements. The Journal of chemical physics 1982;77(7):3654-65.

[22] Hehre W, Ditchfield R,Pople J. Self Consistent Molecular Orbital Methods. XII. Further Extensions of GaussianóType Basis Sets for Use in Molecular Orbital Studies of Organic Molecules. The Journal of Chemical Physics 1972;56(2257.

[23] Barnes S, Brown E, Corrigan N, Coates P, Harkin-Jones E,Edwards H. Raman spectroscopic studies of the cure of dicyclopentadiene (DCPD). Spectrochim Acta A Mol Biomol Spectrosc 2005;61(13-14):2946-52.

[24] M Grimsditch, in *Brillouin Scattering*, Levy, Bass,Stern, Eds. (Academic press, 2001),

[25] Liu X, Sheng X, Lee J,Kessler M. Isothermal cure characterization of dicyclopentadiene. Journal of Thermal Analysis and Calorimetry 2007;89(2):453-7.

[26] Adlhart C, Hinderling C, Baumann H,Chen P. Mechanistic studies of olefin metathesis by ruthenium carbene complexes using electrospray ionization tandem mass spectrometry. J. Am. Chem. Soc 2000;122(34):8204-14.

Chapter 4

Epoxy Cure Kinetics

4.1 Chapter Synopsis

In this study, the cure kinetics of epoxy cured with an amine hardener are investigated using a combination of light scattering techniques. Concurrent Raman and Brillouin scattering are used to monitor the formation of epoxy networks over time both in terms of the structural connectivity of the network as well as the evolution of chemical bonding configurations. The relationship between the elastic properties of the network and the degree of cure was found to depend on the cure temperature and the resin-hardener stoichiometry. A numerical model was created to determine the degree of cure and elastic modulus as a function of time and cure conditions. Accordingly, the modulus of the epoxy comprises two contributions: one directly related to the concentration of covalent bonds that form and another one due to non-bonding interactions that arise as the network relaxes into an optimally packed configuration.

4.2 Introduction

Epoxy resins are commonly used in many industrial applications, particularly as adhesives, protective coatings, and as the matrix material for fiber-

reinforced composites. These applications require a variety of different blends of resins and hardeners and different processing environments (temperature, pressure, etc.) to ensure optimal material characteristics.[1-5] Thermal history, chemical composition, and interfacial effects can all influence the cure behavior of the epoxy, and result in changes in the final chemical and mechanical properties of the cured resin.[6-8] Therefore, it is critical to understand the connection between the processing conditions and the final material properties of the resin in order to ensure optimal performance of the resin in its application. Ideally, these properties should be measurable *in-situ* so that the manufacturing process can be monitored in real time for quality assurance.

Common methods used to determine the cure kinetics and evolution of mechanical properties include differential scanning calorimetry (DSC) and mechanical viscometery.[9-11] Both of these are invasive measurement techniques, and cannot be used to monitor cure *in-situ* under normal manufacturing conditions. DSC places the sample under artificially maintained thermal conditions while viscometers place the sample under external shearing forces, which are not generally present in a curing composite part, and which can cause changes in the structure of a developing polymer network.

Spectroscopic methods, however, are well suited to monitoring polymer cure processes, as they can measure detailed chemical and structural characteristics *in-situ* and without mechanical contact to the sample. Raman light scattering (RLS) measurements allow one to monitor the cure process of epoxy resins. These resins have many active Raman modes, some of which

remain constant during reaction and can be used to normalize spectra and others that change as a result of cure reactions and can be used to monitor polymerization and cross-linking processes that underlie network formation.[12-14] Meanwhile, Brillouin light scattering (BLS) is an invaluable tool in the analysis of network formation, because it is a non-destructive micro-scale probe of the interconnectedness of network components.[15-17] Specifically, it provides a direct optical means to probe the visco-elastic properties of polymer networks under curing conditions. Combining both methods makes it possible to relate the evolution of mechanical properties with the underlying chemical processes that drive polymer network formation.[18]

In this paper, we explore the use of Raman spectroscopy in conjunction with Brillouin spectroscopy as non-destructive *in-situ* methods to analyze the relationship between the chemical degree of cure and the elastic properties of an epoxy resin as it cures under different thermal conditions, and with different epoxy resin-hardener stoichiometric ratios in the initial mixture.

4.3 Experimental Methods

Primary and secondary amines are widely used as curing agents for epoxy resins. The epoxide ring group of an epoxy resin readily reacts with a primary amine. The resulting molecule, now a secondary amine, retains one active hydrogen atom that is free to react with a second epoxide group (Figure 4.1).[19] Therefore when a resin with two or more epoxide groups, reacts with a hardener that has two or more primary amines, or a combination of primary or secondary amines, the result is a highly crosslinked polymer network.

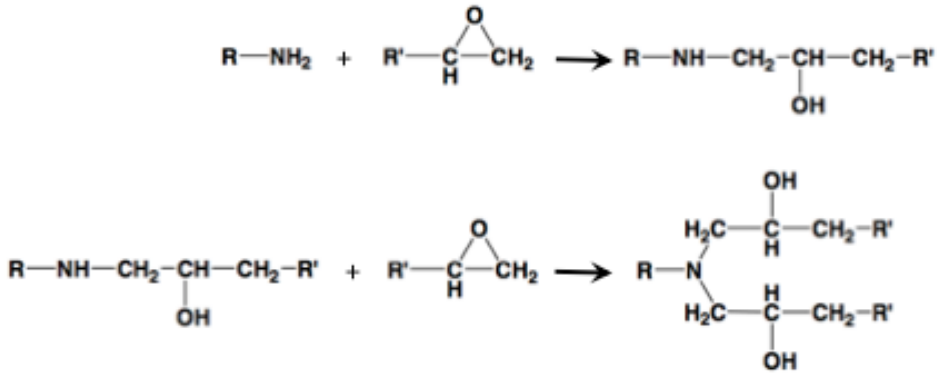

Figure 4.1 Schematic of epoxy reacting with primary and secondary amines

We investigated the cure behavior of epoxy resin as a function of ambient curing temperature, and as a function of the resin to hardener ratio, using a concurrent Raman and Brillouin light scattering. The epoxy system used for this study are Epon 862 resin (Diglycidyl Ether of Bisphenol F, Hexion Specialty Chemicals) mixed with Epikure 9553 amine hardener (proprietary formulation, Hexion Specialty Chemicals). For the temperature dependent measurements, all samples are mixed using the stoichiometric epoxide to amine ratio recommended by the manufacturer. When varying the ratio of resin to hardener, all measurements are carried out at the fixed temperature of 40^{o}C.

To prepare each sample for the light scattering measurements, resin and hardener are added to a glass vial such that the desired concentrations of amine and epoxide are available for reaction. The components are mixed by hand for one minute at room temperature. The mixture is then allowed to stand for an additional minute to allow any trapped gas bubbles that formed during the mixing process to escape. Next, the sample is injected into a sample holder composed of a perforated spacer separating two glass coverslips. The sample fills a

circular aperture with a 20 mm diameter and 2 mm thickness. Finally, the sample holder containing the epoxy is placed in a heating cell on the optical table, which has been pre-heated to the desired reaction temperature. The temperature of the heating cell is monitored using a thermocouple placed less than a millimeter from the sample holder window. The heating cell temperature is controlled using a Eurotherm PID controller. The heating cell is mounted on the optical table such that the center of the sample is positioned in the path of the 532 nm probing laser (Coherent Verdi) and at the focal point of the spectrometer collection optics. The laser power output is fixed at 100 mW for all measurements.

RLS and BLS are similar spectroscopic techniques. Both are inelastic light scattering methods, which measure the shift in energy of scattered light from its incident energy. Both techniques require the sample to be irradiated with monochromatic laser light, and the scattered light to be collected using collimating optics. Once the scattered light is collimated, it can easily be directed to a spectrometer for measurement. Our experimental setup takes advantage of this ability to direct the collimating light, by placing a rotating mirror between the collection lens and the spectrometers. By rotating this mirror we direct the scattered light into either the Raman spectrometer or Brillouin spectrometer. During an experiment, for each time increment, a Raman spectrum is first collected, followed by a Brillouin spectrum. The time logged for each pair of measurements, corresponds to the time at the end of the Brillouin spectrum collection. In this manner, we can attribute measurements from both instruments

to the same 50 μm diameter scattering volume. As a result, we can precisely relate the evolving visco-elastic properties of the sample to its chemical state.

For BLS measurements, we analyze light that inelastically scatters from periodic density waves associated with thermally excited phonons in the sample. The frequency of the scattered light is Doppler-shifted from that of the incident light by an amount ω_b. This shift is related to the speed of sound in the scattering medium, c_L, by the relation $\omega_b = qc$, where q is the wavevector of the scattering phonon, and the subscript associated with the velocity denotes the mode of elastic deformation. Using Brillouin scattering we can detect shear (*S*) and longitudinal (*L*) wave modes, though the particular modes observed depend upon the scattering geometry. [20] The planar periodic nature of the elastic deformation waves establishes a refractive grating, and only scattered light satisfying Bragg's law can be detected, as all other scattered light interferes destructively. This property allows us to select a specific phonon wave vector for measurement, by simply defining the scattering geometry of the incident and collected light. For our experiment, we chose to measure light scattered according to the platelet geometry.[20, 21] In this configuration the incident and scattered light enters and light exists the sample through parallel faces, at an angle that is bisected by a plane parallel to the sample faces (Figure 4.2). This configuration is convenient in that it eliminates the need to know the refractive index of the sample when determining the wavevector of the scattering phonon. In this case, the phonon wavevector is given by $q = 2sin(\theta)/\lambda_0$, where λ_0 is the wavelength of the incident light, and θ is half the angle between the incident and

scattered light. From the wave vector and the Brillouin frequency shift, we calculate the phonon velocity for the sample as

$$c_L = \frac{\omega_b \lambda_0}{2sin(\theta)}. \tag{4.1}$$

From this velocity we can calculate the longitudinal elastic modulus according to

$$M' = \rho c_L^2 = \rho \left(\frac{\omega_b \lambda_0}{2sin(\theta)} \right) \tag{4.2}$$

where ρ is the average density of the sample. All Brillouin spectra were recorded using a Sandercock tandem Fabry-Perot interferometer (TFPI). The mirror spacing used was 5 mm and the scanning range was 200 nm over 512 channels for greater collection speeds. The density of the epoxy system is 1.17 g/cm^3, and is assumed to remain constant during cure.

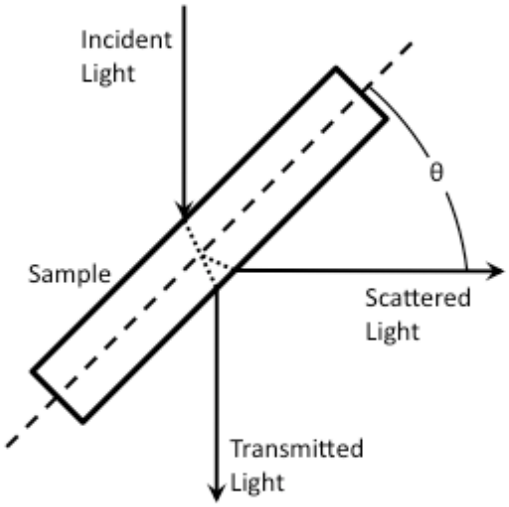

Figure 4.2 Schematic of platelet scattering geometry

Raman scattering is caused by changes in polarizability of the electron density associated with specific chemical bonding configurations while subject to vibrational modes of deformation. The frequency shifts associated with this phenomenon depend on the molecular symmetries and the stresses that the vibrating bonds are subject to, whereas the intensity of the spectral peaks is a measure of the relative abundance of the underlying molecular species. Analysis of the Raman spectra therefore allows us to identify specific molecular structures within a sample and measure their concentrations. For our analysis, we used a Princeton Instruments TriVista triple monochrometer with Princeton Instruments Spec10 liquid nitrogen cooled CCD detector. All spectra are centered at 1275 cm^{-1}, corresponding to the breathing mode of the epoxide ring.[22-24]

Once acquired, Raman spectra are normalized with respect to the 1053 cm^{-1} peak attributed to the phenol rings of the resin, which remain at a constant concentration throughout the cure process. As the epoxide and amine groups react, the epoxide rings are opened resulting in a decrease in the 1275 cm^{-1} peak intensity with respect to the 1053 cm^{-1} phenol peak (Figure 4.3). We therefore calculate the degree of cure (α) using the complement of ratio of the remaining epoxide to the initial epoxide peak intensities, i.e.,

$$\alpha = 1 - \frac{I_{1275}}{I_{1275}^{0}}. \tag{4.3}$$

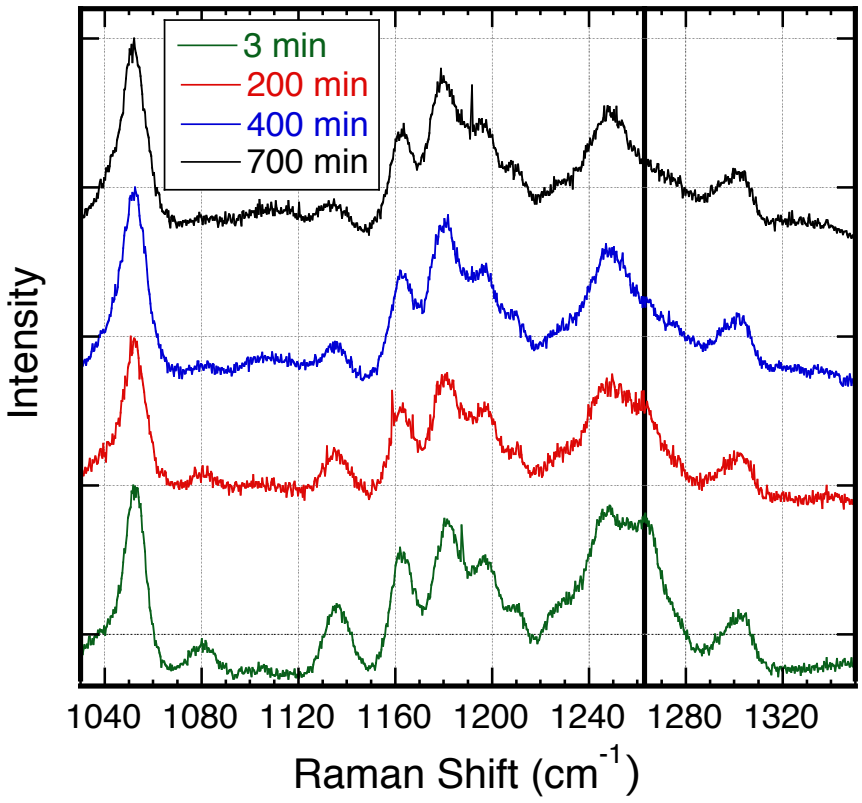

Figure 4.3 Raman spectra are shown for different cure times. The epoxide peak at the marked position shrinks with increasing cure.

4.4 Results and Discussion

To examine the temperature dependence of the cure behavior, experiments were conducted on samples with a 1:1 amine-to-epoxide ratio at four different temperatures (22, 30, 40, and 50 °C). The light scattering results show that the degree of cure exhibits the characteristic S-shaped dependence on time, common to curing systems (Figures 4.4a). As expected, the rate of cure increases with temperature. It is important to note that the degree of cure reaches a maximum slightly above 70% cure. At this point, the remaining reactive groups lack the mobility required to continue the reaction. Furthermore, the initial upward curvature of the cure curve, especially noticeable at lower

temperatures, suggests that the reaction is self-accelerating. This behavior could be attributed to local thermal changes due to the exothermic nature of the reaction, chemical self-catalysis, formation of local inhomogeneities, and the manifestation of gel effects within the sample. [25] Local heating in our sample is not a likely cause of self-acceleration due to the high surface area to volume ratio of our sample. Indeed, simulations of cure temperatures of a sample with the same composition and similar dimensions to ours show negligible variation during cure.[7]

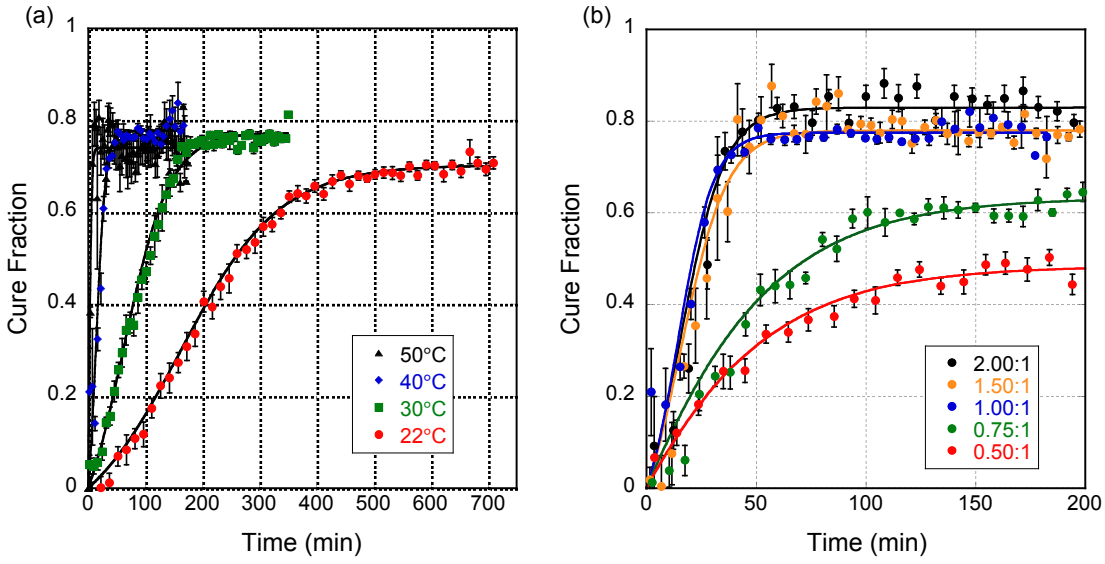

Figure 4.4 Degree of cure is shown as a function of time, along with best-fit curves for different cure temperatures (a) and different stoichiometries (b).

In order to quantify the reaction kinetics of the system, we analyzed the cure curves using several reaction models. The generalized form of these kinetic models is

$$\frac{d\alpha}{dt} = k(t)f(\alpha) \tag{4.4}$$

where α is the degree of cure and *k* is a temperature dependent rate constant that follows Arrhenius's equation:

$$k = He^{\left(-\frac{E_a}{RT}\right)} \tag{4.5}$$

with *H* being a constant, E_a the activation energy, and *R* the ideal gas constant. This can be rewritten as

$$ln(k) = -\left(\frac{E_a}{R}\right)\left(\frac{1}{T}\right) + ln(H) \tag{4.6}$$

Accordingly, when plotting *ln*(*k*) vs. 1/*T*, the quantities *H* and E_a/R emerge as the intercept with the ordinate and the slope of a linear fit to the data points.

Several forms of f(α) have been demonstrated to satisfactorily describe epoxy cure behavior.[10, 25-29] A summary of these models is given in Table 4.1. As a basis of inquiry, we systematically fit our cure data using each of the models described in this table, and determined the reaction order, acceleration term, and inhibition terms needed to best describe our data. In all of models α_∞ is the degree of cure at t = ∞. With values of less than 1 it acts as a limiting term reflecting the fact that complete cure cannot be achieved due to the loss of mobility of reactive groups at high degrees of cure. Our analysis reveals that, based on the value of the correlation coefficient R^2, the cure reaction is best described as a first order reaction with self accelerating properties. This confirms the mechanism suggested by the general shape of the cure curve. The Arrhenius behavior of *ln*(*k*) vs. 1/*T* is evident in Figure 4.5. From this plot we extracted the rate constant and activation energy, the values of which are summarized in Table 4.2. The acceleration constant, *C*, is not temperature

dependent, and has an average value of 8.12. The final degree of cure is also temperature independent, with an average value of 0.75.

Reaction Model	F(α)	R^2
1st order	$(\alpha_\infty - \alpha)$	0.954
2nd order	$(\alpha_\infty - \alpha)^2$	0.912
nth order	$(\alpha_\infty - \alpha)^n$	0.954
Self accelerated 1st order	$(\alpha_\infty - \alpha)(1 + C\alpha)$	0.984
Self accelerated 2nd order	$(1 - \alpha)(\alpha_\infty - \alpha)(1 + C\alpha)$	0.980

Table 4.1 Summary of cure models and qualities of fit

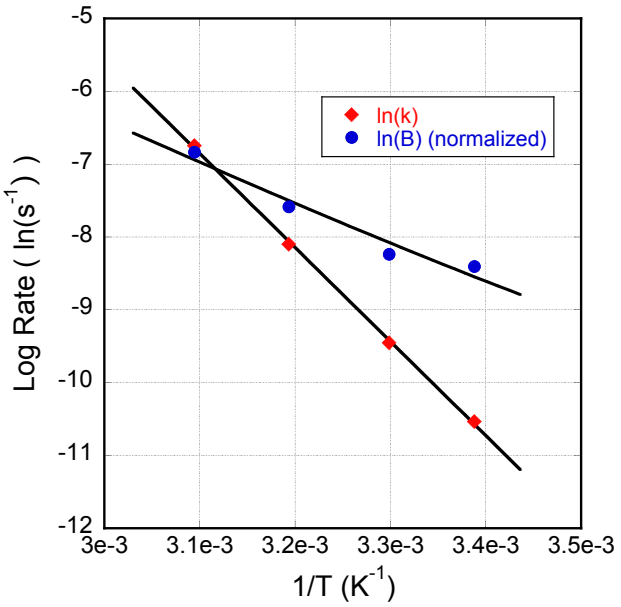

Figure 4.5 Arrhenius plot for the reaction rate coefficient k and the relaxation rate coefficient B. The values of the relaxation rate coefficient have been normalized by the change in modulus due to relaxation at each temperature. This normalization allows us to compare the reaction and relaxation rates on the same scale.

	Ln(H)	E_a	α_∞	C
Cure Model	33.165	107.3 kJ/mol	0.75	8.12

Table 4.2 Cure model parameters

We used the same first order self-accelerating cure model to fit the cure data for the measurements conducted with different amine concentrations. The amine to hardener ratios that we investigated are 0.5:1, 0.75:1, 1:1, 1.5:1, and 2:1. All of these experiments were conducted at a temperature of 40^{o}C. In fitting this data we used the value for *k* determined by the Arrhenius fit from the temperature study, because the underlying chemistry of the reaction should remain the same for different reactant concentrations. The final degree of cure, $\alpha_{\infty,}$ depends strongly on the resin-to-hardener ratios, as is shown in Figure 4.6. For amine concentrations less than 1:1, the final degree of cure increases linearly with amine concentration. In these reactions the process is limited by the availability of amine, and as such, when the amine is used up, the reaction stops. Above the stoichiometric ratio, the final degree of cure is roughly constant. In this case the epoxy availability limits the reaction, and so the final degree of cure no longer depends on the amine concentration.

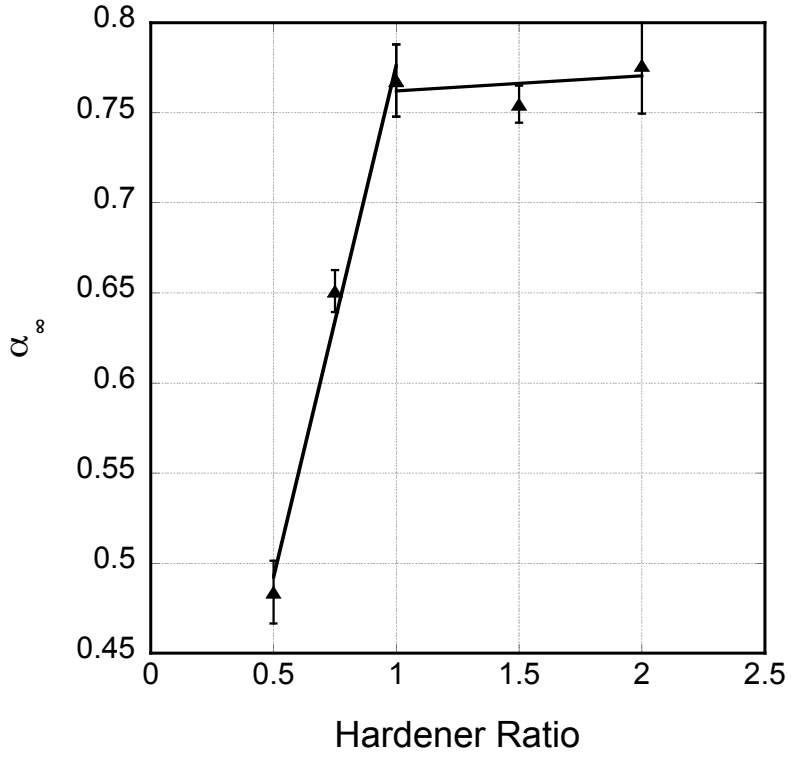

Figure 4.6 Final degree of cure (α_∞) as a function of hardener to epoxide ratio

The value of the acceleration constant, *C*, changes both above and below the 1:1 amine-to-epoxide ratio. For the 1:1 ratio, the value of C is the same as observed for the samples cured at different temperatures. Below 1:1 the value of C becomes small, with an average value of 0.75. This value effectively minimizes the self-accelerating effect and causes the reaction to behave much like a typical first order reaction. Above the 1:1 ratio the value of *C* is also decreased, though not by as much as the below-stoichiometric hardener concentrations. Again, the value of *C* remains roughly constant for the above stoichiometric hardener concentrations and averages at 5.33. The behavior of the self-acceleration coefficient *C* observed for off-stoichiometric resin-hardener ratios supports the notion that this this effect is due to steric accessibility of reacting partners within the sample rather than local heating. The hardener has a

higher reaction site concentration per unit volume than the epoxy resin, so significantly increasing the hardener concentration does less to dilute the active reaction than increasing the relative amount of epoxy does.

Using Brilluoin scattering we monitor the longitudinal modulus of the epoxy as it cures. The overall behavior of the modulus appears comparable to the cure behavior for samples both at different temperatures and different stoichiometries as seen in Figures 4.7,a-b. Because we collected our cure and modulus data concurrently from the same scattering volume, we can directly relate these two quantities. In Figures 4.8 a-b we plot the longitudinal modulus vs. the degree of cure for both different cure temperatures and for different resin-hardener stoichiometries. We note that the elastic modulus depends almost linearly on cure for the samples when cured at the slowest reaction rates, whether this rate is controlled via the temperature or the hardener-to-resin ratios. Note that in the latter case, i.e., at low hardener concentrations, the final degree of cure varies, but the end points in the modulus vs. degree of cure data still fall onto a line connecting the modulus of pure resin with that of the most rigid network. At faster reaction rates the elastic modulus appears to lag behind the formation of the polymer network structure, as judged by the degree of cure.

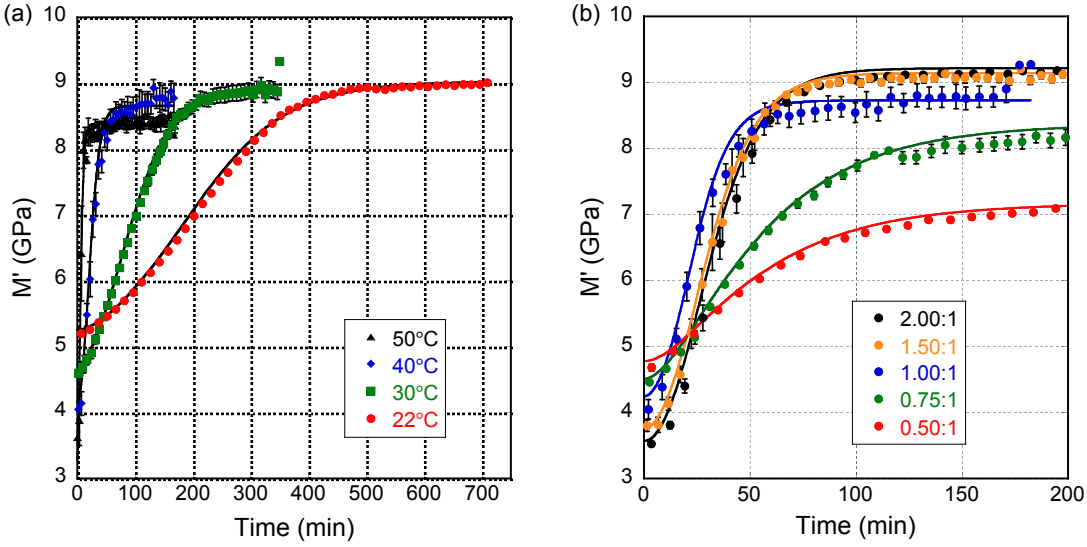

Figure 4.7 Longitudinal elastic modulus as a function of time for different cure temperatures (a) and different sample stoichiometries (b).

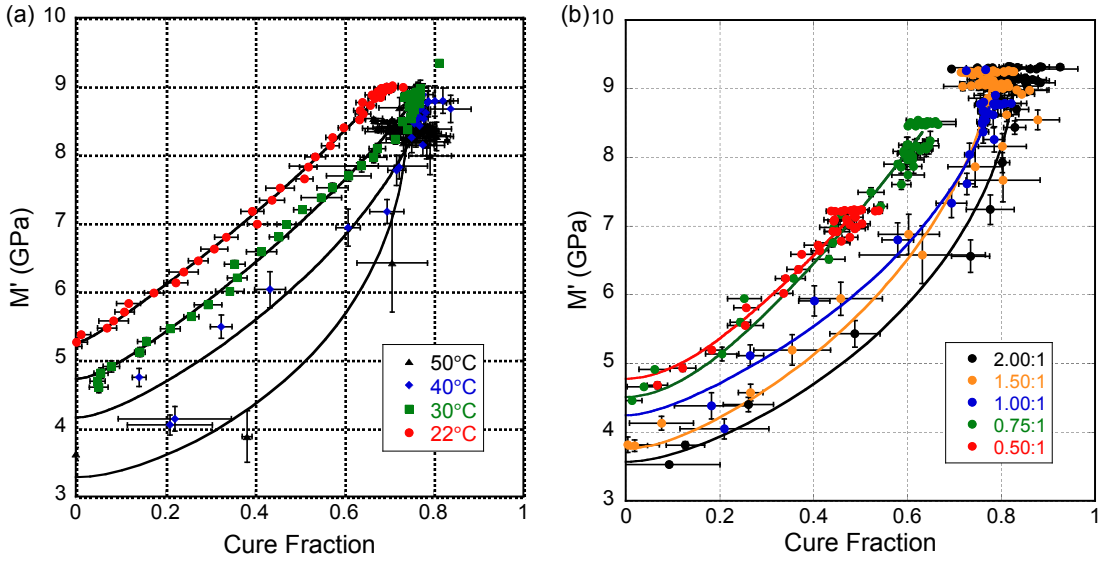

Figure 4.8 Longitudinal elastic modulus as a function of cure for different cure temperatures (a) and different sample stoichiometries (b).

During cure, the reacting epoxy forms a covalently bonded network that is responsible for part of the observed change in elastic properties. Based on our findings, the elastic modulus of this network depends not only on the number and

topology of its constituent bonds, but also on the configuration and packing efficiency of network segments, possibly, the sequence by which the linkages between these segments are formed. It is reasonable to assume that during cure, the location in which any given bond forms is not necessarily optimal for the overall network configuration. Instead, the network structure likely reorganizes during and even after the cure reaction until it reaches an equilibrium state.[30] This reorganization may facilitate the formation of additional covalent bonds, or simply result in an optimized molecular packing that provides for stronger overall non-bonded dispersive interactions. In the case of our epoxy system, we submit that the nonlinearity in the modulus as a function of the degree of cure for the faster polymerization is evidence for this reorganization process, and in the following present evidence for this process to predominantly consist of structural relaxation that leads to improved van der Waals and hydrogen bonding between polymer segments. Indeed, when polymerization reactions are slow, this post-polymerization structural reorganization occurs at a rate similar to or faster than the cure process itself. In this case, the network structure remains roughly at equilibrium throughout the cure process. Conversely, when the polymerization reaction occurs quickly, the network formation outpaces the structural reorganization resulting in the observed nonlinear relationship between the modulus and the degree of cure. The fact that the modulus increases during this relaxation process means that additional stabilizing molecular interactions develop. To gain further information about the nature of these interactions, we develop a model that describes the observed time-dependence of the elastic

modulus relative to that of the degree of cure. *A priori*, this model does not require specification of the type of this secondary bonding, but we rather deduce this from the ensuing fit parameters. The model therefore describes equally well the network formation resulting from two or more competing chemical reaction mechanisms or from locally sequential network evolution processes such as bond formation followed by network relaxation towards an optimally packed structure.

Our objective in developing this model is to capture how a variation in reaction-rate, as monitored using Raman scattering, affects the mechanical behavior of the resulting network. We assume that for a given degree of cure, the network will reach the same modulus given enough time for the structure to fully develop and relax to a local energy minimum. This is based on the observation that the modulus of fully cured samples is the same for all curing rates. Furthermore, we assume that the equilibrium (or fully relaxed) modulus is a linear function of the degree of cure, i.e., $M' = M'_0 + \left(M'_\infty - M'_0\right)\left(\alpha/\alpha_\infty\right)$. This is based on the observation that for the low-temperature curing reactions and for the hardener ratios below 1:1, the moduli evolve nearly linearly with the degree of cure. We then let the rate of change of the modulus depend on a linear combination of two terms: one is linked to the rate of formation of covalent bonds and the other is proportional to the difference between the instantaneous modulus and the equilibrium modulus for the current degree of cure. The rate equation describing this behavior is

$$\frac{dM'}{dt} = A\frac{d\alpha}{dt} + B\left(M'_0 + \frac{\alpha(M'_\infty - M'_0)}{\alpha_\infty} - M'\right). \tag{4.7}$$

Here *A* reflects the contribution of the network of covalent bonds to the epoxy stiffness, and *B* is a measure of the network relaxation rate. M'_0 and M'_∞ denote elastic modulus of the system at the beginning and at the end of the cure process, and α_∞ is the final degree of cure for the system.

Both the initial and final longitudinal moduli of our epoxy system decrease linearly with increasing temperature. Fully cured samples that have been allowed to cool to room temperature all exhibit the same modulus, within measurement error, regardless of the temperature at which they were cured. Similarly, when taking a sample that was first fully cured at room temperature and heating it to various elevated temperatures, its modulus drops to the same value as that of a sample cured and held at these elevated temperatures. This is illustrated in Figure 4.9, which shows both the M'_0 and M'_∞ measured for samples cured at different temperatures, as well as the modulus of a sample cured at room temperature and afterwards heated to 50°C. The moduli coincide within measurement error, independent of thermal history. This demonstrates that the decrease in modulus of the samples cured at higher temperature is solely due to the increased thermal motion of network components and entirely reversible structural changes, rather than to an irreversible change in the intrinsic bonding pattern within the polymer network. The optimal value for the network modulus, *A*, has been determined as 1.625 GPa. At maximum cure this value accounts for an increase of about 1.14 GPa beyond the bulk modulus, K = 5.22 GPa, which we assume to be the only contribution to M' at zero cure. Hence, using the value

of 6.36 GPa for M'_T of the fully cured epoxy, we obtain for the Young's modulus $E_T = 9K\left(M'_T - K\right)/\left(M'_T + 3K\right)$ = 2.43 GPa, which is close to the literature value of 2.55 GPa (as per specification by Hexion Specialty Chemicals). Note that in our model the covalent bond contributions to the elastic response can be almost entirely attributed to the isothermal modulus, as is discussed in more detail below. Hence, the subscript *T* in the above formulas refers to isothermal elastic constants. The quantities measures using Brillouin scattering are adiabatic constants. (We omit a subscript with these quantities for simplicity sake.)

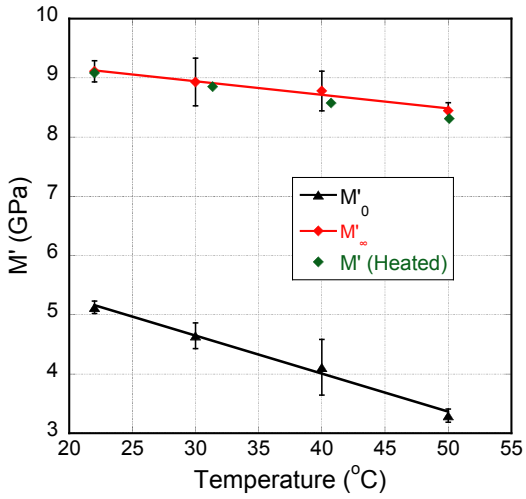

Figure 4.9 Initial and final longitudinal moduli (M'_0 and M'_∞) as functions of temperature, as well as the longitudinal modulus of a sample cured at room temperature and heated to 50 °C

Figure 4.5 shows the relaxation rate, *B*, compared to the reaction rate coefficient *k*. Because *B* and k each describe the rate of change of two quantities with different units and magnitudes of overall change, they each have been normalized with respect to the total change in modulus and degree of cure, respectively, that occur at each temperature. This normalization allows us to

compare B with k in terms of the relative changes they effect. Note that this normalization does not affect the temperature dependence of these factors. We observe that the rate constant B increases with temperature, following Arrhenius behavior with an activation energy of E_{aR} = 57.1 kJ/mol. Accordingly, the network reorganization rate is higher at increased temperatures, which allows the network to access an equilibrium state more rapidly. Importantly, however, with an activation energy of 107.3 kJ/mol, the temperature dependence of the reaction rate coefficient is much stronger than that of the relaxation rate coefficient, which accounts for the fact that at room temperature the relaxation rate is much higher than the reaction rate, and the measured modulus therefore closely adheres to that of an ideally relaxed structure. With increasing temperature the two rates become more closely matched, and thus gradually revealing the relaxation process. At the highest temperature the reaction rate slightly surpasses the relaxation rate, exposing the latter process as the rate-limiting step in network formation.

The initial modulus of the amine-epoxy resin mixture decreases linearly with increasing hardener concentration, which reflects the thinning effect of the hardener. Pure resin is very viscous, and as hardener is added it reduces the viscosity of the system, which explains the lower initial modulus. Conversely, the behavior of the final longitudinal modulus exhibits two regimes with respect to the hardener concentration. Below the stoichiometric ratio, the network connectivity is limited by amine availability. As a result, the final degree of cure increases linearly with increasing amine concentration, and so does the final elastic

modulus. Above the stoichiometric ratio, increasing the amount of amine no longer advances network connectivity, and only a small increase in the final modulus is observed. The initial and final moduli for each hardener concentration examined are shown in Figure 4.10. Eq. (4.7) also fits the modulus data for the samples cured with different resin-to-hardener ratios. Since these systems were all cured at the same temperature, rate changes are only affected by structural mobility and the probability of juxtaposition of reactive sites. We observe that the relaxation rate constant *B* remains constant with an average value of 10^{-3} s^{-1} over the range of hardener concentrations tested. When fitting the reaction rate coefficient, *k*, within experimental error we find for all compositions the same value as the one determined at 40˚C when investigating the effect of temperature on cure at the stoichiometric resin-to-hardener ratio.

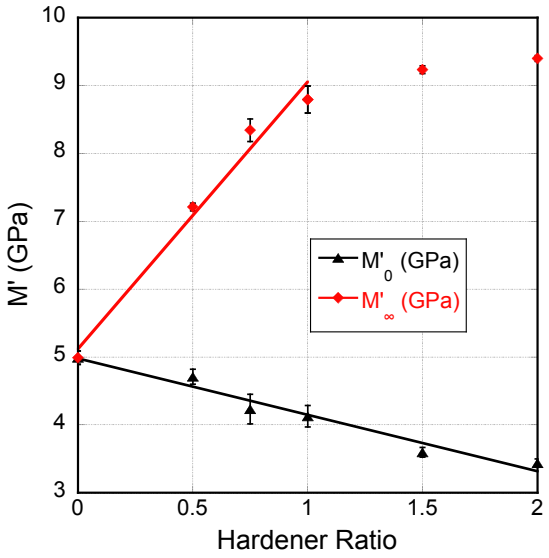

Figure 4.10 Initial and final longitudinal moduli (M'_0 and M'_∞) as functions of sample stoichiometry

In the series for different resin-to-hardener ratios we control the reaction rates by changing the probabilities for steric encounter, without affecting the magnitude of the reaction rate coefficients. The relaxation rate, on the other hand, may be affected due to the change in mobility of the molecular constituents, depending on the mixing ratio. When the system cures with a resin-to-hardener ratio below 1:1 the reaction is amine limited resulting in a less densely bonded network structure and reduced mechanical properties. Above the stoichiometric ratio, only modest changes in the reaction kinetics or the elastic properties are observed. Similar to the effect of temperature, when accelerating the cure rate by increasing the hardener concentration, the relaxation process, whose rate is little or not at all affected by the concentration of hardener, eventually becomes apparent at high cure rates. Not tested were stoichiometries where the volume of the epoxy and hardener are similar, and there are a vastly greater number of amine groups than epoxides. In this regime it is likely that both the cure kinetics and the elastic properties will be dramatically different as the hardener will act as a solvent for the epoxy network as well as a reaction component. However, such a scenario is unlikely and less relevant in practice.

To successfully describe the evolution of the elastic modulus as a function of the degree of cure, it was necessary to account for two contributions: that of a network of covalent bonds and that due to optimized packing of polymer segments. The latter can be modeled as a relaxation process. It is important to note that the reason why these two mechanisms are discernable in this

investigation is the high frequency of the phonon probed with Brillouin scattering. Accordingly, we measure the adiabatic elastic modulus, whereas static tensile testing measures the isothermal modulus. The latter corresponds to that of the fully disentangled structure under the influence of an applied stress. The difference between adiabatic and isothermal modulus is called relaxational modulus. For the epoxy system investigated here, the relaxational longitudinal modulus amounts to approximately 3.1 GPa. This additional capacity to store elastic energy can be attributed to the optimization of polymer packing, maximizing non-covalent interactions between network segments. This packing relaxation does not affect the network topology and is reversible. Hence the fully relaxed network exhibits the highest (adiabatic) modulus, as probed by Brillouin scattering. Conversely, static tensile testing probes a lower (isothermal) modulus, which corresponds to a non-relaxed network (or network constrained by the applied stress).

4.5 Conclusion

This work demonstrates the use of concurrent Raman-Brillouin light scattering measurements to characterize the relationship between the cure kinetics of an epoxy resin and the mechanical properties that develop as a result of the cure process. From these measurements we have developed a numerical model that captures the observed curing behavior. Our results show that for a given maximum degree of cure, the resulting epoxy network exhibits the same mechanical properties. The elastic modulus of the epoxy network consist of two contributions: that of a network of covalent bonds and that of non-bonded

interactions between network segments, which arise when the structure relaxes into an optimally packed configuration. The latter is associated with the so-called relaxational modulus in visco-elastic theory. By probing high-frequency phonons, Brillouin scattering allows one to resolve this relaxational modulus, which is an attribute of a structure in its energy minimum. Static tensile testing, on the other hand, does not resolve the relaxational modulus, as it measures the elastic properties of a structure constrained by the applied stress. Structural changes between relaxed and strained networks are reversible. With increasing rate of cure, the relaxational aspects of network formation become more apparent, because the relaxation process becomes rate limiting in reaching the equilibrium configuration of the network structure.

4.6 References

[1] Chu B,Wu C. Structure and dynamics of epoxy polymers. Macromolecules 1988;21(6):1729-35.

[2] Dušek K. Network formation in curing of epoxy resins. Epoxy Resins and Composites III 1986;1-59.

[3] Lemay J,Kelley F. Structure and ultimate properties of epoxy resins. Epoxy Resins and Composites III 1986;115-48.

[4] Meyer F, Sanz G, Eceiza A, Mondragon I,Mijovi J. The effect of stoichiometry and thermal history during cure on structure and properties of epoxy networks. Polymer 1995;36(7):1407-14.

[5] Riccardi CC, Adabbo HE,Williams RJJ. Curing Reaction of Epoxy Resins with Diamines. Journal of Applied Polymer Science 1984;29(2481-92.

[6] Heinrich C, Aldridge M, Wineman A, Kieffer J,Waas AM. Integrated Computational Materials Science and Engineering of Textile Polymer Composites. Proceedings of the 52nd AIAA/ASME/ASCE/AHS/ASC structures, structural dynamics, and materials conference. Denver, Colorado, USA 2011;

[7] Heinrich C, Aldridge M, Wineman AS, Kieffer J, Waas AM,Shahwan KW. Generation of heat and stress during the cure of polymers used in fiber composites. International Journal of Engineering Science 2012;53(85-111.

[8] Heinrich C, Aldridge M, Wineman AS, Kieffer J, Waas AM,Shahwan KW. The role of curing stresses in subsequent response, damage and failure of textile polymer composites. Journal of the Mechanics and Physics of Solids 2013;61(5):1241-64.

[9] Matejka L. Rheology of epoxy networks near the gel point. Polymer Bulletin 1991;26(1):109-16.

[10] Halley PJ,Mackay ME. Chemorheology of thermosets-an overview. Polymer Engineering & Science 1996;36(5):593-609.

[11] O'Brien DJ, Mather P,White S. Viscoelastic properties of an epoxy resin during cure. Journal of composite materials 2001;35(10):883.

[12] Aust JF, Booksh KS, Stellman CM, Parnas RS,Myrick ML. Precise Determination of Percent Cure of Epoxide Polymers and Composites via Fiber-Optic Raman Spectroscopy and Multivariate Analysis. Appl. Spectrosc. Applied Spectroscopy Appl. Spectrosc. 1997;51(2):247-52.

[13] Chike KE, Myrick ML, Lyon RE,Angel SM. Raman and Near-Infrared Studies of an Epoxy Resin. Appl. Spectrosc. Applied Spectroscopy Appl. Spectrosc. 1993;47(10):1631-5.

[14] Lyon RE, Chike KE,Angel SM. In situ cure monitoring of epoxy resins using fiber-optic Raman spectroscopy. Journal of Applied Polymer Science 1994;53(13):1805-12.

[15] Müller U *et al.* Acoustic profilometry of interphases in epoxy due to segregation and diffusion using Brillouin microscopy. New Journal of Physics 2008;10(2):023031.

[16] Philipp M, Müller U, Riobóo R, Baller J, R ,. Interphases, gelation, vitrification, porous glasses and the generalized Cauchy relation: epoxy/. New Journal of Physics 2009;

[17] Yamura H, Matsukawa M, Otani T,Ohtori N. Brillouin scattering study on the elastic properties of epoxy adhesive layer. Jpn. J. Appl. Phys., Part 1999;1(38):3175.

[18] Aldridge M *et al.* Combined Experimental and Simulation Study of the Cure Kinetics of DCPD. Journal of Composite Materials 2010;44(22):2605-18.

[19] Xu L, Fu JH,Schlup JR. In Situ Near-Infrared Spectroscopic Investigation of the Kinetics and Mechanisms of Reactions between Phenyl Glycidyl Ether (PGE) and Multifunctional Aromatic Amines. Industrial & Engineering Chemistry Research 1996;35(3):963-72.

[20] Kruger J, Peetz L,Pietralla M. Brillouin scattering of semicrystalline poly(4-methyl-1-pentene): study of surface effects of bulk and film material. Polymer 1978;19(12):1397-404.

[21] M Grimsditch, in *Brillouin Scattering*, Levy, Bass,Stern, Eds. (Academic press, 2001),

[22] Merad L *et al.* In-situ monitoring of the curing of epoxy resins by Raman spectroscopy. Polymer Testing 2009;28(1):42-5.

[23] Mertzel E,Koenig J. Application of FT-IR and NMR to epoxy resins. Epoxy Resins and Composites II 1986;73-112.

[24] Riegel B, Kiefer W, Hofacker S,Schottner G. FT-Raman Spectroscopic Investigations on the Organic Crosslinking in Hybrid Polymers. Part I: Model Reactions of Simple Epoxides. Appl. Spectrosc. Applied Spectroscopy Appl. Spectrosc. 2000;54(9):1384-90.

[25] Malkin A,Kulichikhin S. Rheokinetics of curing. Polymer Compositions Stabilizers/Curing 1991;217-57.

[26] Maiti S, Shankar C, Geubelle P,Kieffer J. Continuum and Molecular-Level Modeling of Fatigue Crack Retardation in Self-Healing Polymers. Journal of Engineering Materials and Technology 2006;128(595.

[27] Malkin AY, Kulichikhin SG, Kerber ML, Gorbunova IY,Murashova EA. Rheokinetics of curing of epoxy resins near the glass transition. Polymer Engineering & Science 1997;37(8):1322-30.

[28] Reghunadhan Nair CP,Ninan KN. Rheological cure characterization of phosphazene-triazine polymers. Journal of Applied Polymer Science 2003;88(4):908-14.

[29] Zlatanic A, Dunjic B,Djonlagic J. Rheological study of the copolymerization reaction of acrylate-terminated unsaturated copolyesters with styrene. Macromolecular Chemistry and Physics 1999;200(9):2048-58.

[30] Andjelic S, Fitz B,Mijovic J. Reorintational Dynamics and Intermolecular Coorperativity in Reactive Polymers. 2. Multifunctional Epoxy-Amine Systems. Macromolecules 1997;30(5239-48.

Chapter 5

In-situ elastic modulus of epoxy between carbon fibers

5.1 Chapter Synopsis

The mechanical properties of thermoset resins used in carbon fiber composites depend on their processing conditions. The inclusion of fibers into the resin locally affects the thermal balance, creates chemical inhomogeneities, and templates structural developments in the polymer near the fiber surface. In this study we use Raman and Brillouin light scattering to investigate the effect of carbon fibers on the mechanical properties of an epoxy matrix. Our results show that the longitudinal modulus of epoxy within a fiber tow is about 3.75% lower than the modulus of the epoxy outside of the tow. Furthermore, within a fiber tow, the modulus depends on the local packing density of the carbon fibers. Comparison between our Brillouin and Raman measurements suggest that the observed spatial inhomogeneity in elastic properties of the matrix is not a result of residual stresses within the matrix but more likely due to structural reorganization in the interfacial region.

5.2 Introduction

Polymer matrix composites are becoming materials of choice for constructing stiff, lightweight parts for a range of applications from aerospace and

automotive components, to sporting goods. However, designing a composite part is significantly more challenging than for an equivalent part made of a single material. The mechanical properties of the composite are determined according to the properties of constituent materials and the processing conditions, such as mixing procedure, forming rates, temperature, and pressure used in manufacturing the composite. It is vital to understand how these processing conditions affect the final properties of the composite in order to optimize the performance of a manufactured part.

In the case of a thermoset matrix textile composite, a liquid polymer resin is forced into the interstitial spaces of the reinforcing textile and cured under controlled temperature and pressure conditions. In the bulk, a resin cures with limited constraints on shrinkage or diffusion. However when inclusions in the form of textile fibers are added to the polymer, they obstruct the free flow of the resin while it is still in liquid form. The surface of the reinforcing constituent has been demonstrated to alter the cure kinetics and final mechanical properties of the polymer network.[1, 2] Volumetric constraints cause significant stress formation during the cure of thermoset resins.[3] Furthermore, fiber bundles within a composite can constrict the curing resin so that it causes microcracking of the resin matrix by the end of cure.[4, 5] Finally, if the fibers have different heat conduction characteristics than the resin, thermal conditions for the curing of the resin will also be different from those observed in the bulk. [6, 7]

A good representative system for exemplifying this behavior is a carbon fiber textile composite with an epoxy matrix material. In this system the matrix is

composed of two parts: an epoxy resin, and an amine hardener. These components are mixed and polymerize exothermically to produce a highly crosslinked network around the carbon fibers. In these systems, it has already been observed that the mechanical behavior of the composites is not well modeled using the bulk properties of the constituent epoxy and carbon fibers.[8] Finite element modeling of both metal and polymer matrix composites has shown that the shape and packing of fibers has an effect on the mechanical properties of a tow. [9-11] All of these studies demonstrate the need for further mechanical characterization of the matrix material within a fiber tow.

The small length scale at which the mechanical properties must be measured complicates characterization of the epoxy matrix within a composite. Common measurements of the elastic properties of polymer matrices rely on mechanically probing the sample surface. However, mechanical probes can be difficult to use in the confined spaces of a fiber tow. For example, nanoindentation close to the fiber-polymer interface is affected by the confinement of the matrix material near the interface, resulting in an artificially higher measured stiffness. [12] Brilluoin light scattering measurements using microscope optics has been shown to resolve the mechanical behavior of materials at the micron scale.[13, 14] Brillouin scattering probes the propagation and attenuation of thermal phonons that exist in all condensed matter at finite temperature. Therefore, no physical actuation is necessary to measure the elastic modulus. Additionally, the thermodynamic equilibrium of the sample is not disturbed because the momentum exchanged between the phonon and probing

photon is small compared with the original phonon momentum. Deformations that would interfere with the mechanical constraints of material near fibers are not required, and thus, confinement of matter in narrow spaces is not an issue for this technique. Furthermore, this technique can easily be combined with other optical analyses such as micro-Raman scattering, which is widely used as a tool for measuring structural deformations due to imposed or residual stress within a sample.[15-17] Because both methods are based on light scattering, their spatial resolution is primarily limited by the wavelength of light used. This enables measurements to be made in tightly confined regions and near interfaces.

In this investigation, we use Brillouin and Raman light scattering to measure the longitudinal modulus and residual stresses in the epoxy matrix of a carbon fiber reinforced composite. Our measurements reveal that the elastic response of the epoxy depends on its location relative to the fibers. Outside of fiber tows, the elastic modulus is close to that of bulk epoxy, cast without fibers, whereas within a fiber tow the modulus is linearly correlated with the local density of fibers surrounding the measurement spot. At the same time, our Raman measurements show that there is little connection between these changes and any existing residual stresses within the sample.

5.3 Methods and underlying formalisms

The composite system we chose for our study consists of eight layers of 45° braided carbon fibers embedded in a matrix of epoxy resin. The resin used is Epon 862, which was hardened with Epikure 9553, both manufactured by Hexion Specialty Chemicals. The average fiber diameter in our samples is 6 μm. Cubic

samples were cut from the composite and mounted for polishing such that the axial tows lay parallel to the polishing plane. The sample was then polished using progressively finer compounds, ending with 0.25 μm SiC. The result of the polishing is a sample surface that appears smooth at 100x magnification on our microscope. For comparison, we also prepared bulk epoxy samples that were cut and polished in the same manner as the composite samples.

Our samples were imaged with an Olympus IX71 inverted microscope using a 100x objective lens. The field of view on the sample at this magnification measures 49 μm by 37 μm. Laser illumination for light scattering is provided by a 532 nm Coherent Verdi V2 laser through the objective lens. The laser spot size has a diameter of ~1.5 μm. Laser power at the sample is set to 0.5 mW. Scattered light is collected by the objective lens and exits through the back of the microscope. The scattered light is then directed to either the Brillouin spectrometer or the Raman spectrometer by repositioning a motorized mirror. The Brillouin light scattering measurement consists of analyzing the light scattered from thermal phonons that naturally exist within matter at finite temperature. A small fraction of these scattering events occur inelastically, emitting photons with a frequency shift proportional to the phonon propagation velocity. Moreover, considering that phonons constitute a density, and consequently a periodic and planar refractive index grating, light scattered from this grating must obey the Bragg diffraction condition, $\pm \boldsymbol{q} = (\boldsymbol{k}_s - \boldsymbol{k}_i)$ (Eq. 2.1), where $\boldsymbol{q}$ is the wavevector that describes the wavelength and propagation direction of the phonons probed, also called the scattering vector, and $\boldsymbol{k}_s$, and $\boldsymbol{k}_i$,

are wavevectors of the scattered and incident light, respectively. Accordingly, the choice of scattering geometry allows one to single out phonons that propagate in a particular direction, and thereby ascertain the orientation of the underlying longitudinal and shear deformation. Because the velocity of sound is much smaller than the velocity of light, we can approximate $|\boldsymbol{k_s}| = |\boldsymbol{k_i}| = \frac{n}{\lambda_0}$ (EQ. 2.2). Here, *n* is the index of refraction of the sample and λ_0 is the wavelength of the incident light. From this approximation we calculate the magnitude of $\boldsymbol{q}$ as $|\boldsymbol{q}| = \frac{2n}{\lambda_0} sin\left(\frac{\theta}{2}\right)$ (Eq. 2.3) where θ is the angle between $\boldsymbol{k_s}$ and $\boldsymbol{k_i}$. Experimentally the scattering vector is determined by the laser wavelength and the angle between the illumination and collection optical paths. Because we use the same objective to illuminate the sample and to collect the scattered light, the scattering angle for our measurements is 180°. The phonon velocity of the medium can be calculated using the scattering vector, and the measured the frequency shift of the scattered light using $v = \frac{\Delta\omega}{|\boldsymbol{q}|} = \frac{\Delta\omega\lambda_0}{2nsin\left(\frac{\theta}{2}\right)}$ (Eq. 2.8), where Δω is the frequency shift of the scattered light. From this calculation we can then directly determine the longitudinal elastic modulus using the relation

$$M' = \rho v^2 = \frac{E(1-\nu)}{(1+\nu)(1-2\nu)}, \quad (5.1)$$

Here *E* is the Young's modulus, ν is the Poisson's ratio, and ρ is the sample mass density. We collected all of our Brillouin spectra using a Sandercock six-pass tandem Fabry-Perot interferometer. [18] The spectrum of scattered light was analyzed by fitting the collected data with the appropriate expression of the dynamic structure factor using the open source peak fitting software package

Fityk. [19, 20] This yields peak position, i.e., the frequency shift , the peak intensity, and its full width at half maximum.

Whereas Brillouin scattering yields a measure of the stiffness of a sample, Raman scattering provides information about the deformation of the polymer network in a sample. Studies have demonstrated that the symmetrical stretching mode of phenylene around 1600 cm^{-1} is sensitive to the state of stress in a polymer. [15-17] As the tensile stress applied to the ring is increased, the peak shifts monotonically to a lower wavenumber. Furthermore, it has been found that the D and G bands in the Raman spectrum of carbon fiber shift to lower wavenumbers under the application of tensile stress. [17, 21] The epoxy that we chose for our composite, Epon 862, contains two phenylene groups, which yield a cluster of three peaks between 1585 cm^{-1} and 1618 cm^{-1} (Figure 5.1 (a)). By analyzing the position of these peaks along with the locations of the D and G peaks of the carbon fiber spectrum (Figure 5.1 (b)), we can determine the state of stress of our sample relative to bulk epoxy and loose carbon fibers. We collected the Raman spectra using a Princeton Instruments TriVista triple monochrometer with a 750 mm focal length, paired with a Princeton Instruments Spec 10 liquid nitrogen cooled CCD detector. Collections were centered at 1600 cm^{-1} for regions composed both of epoxy and carbon fibers.

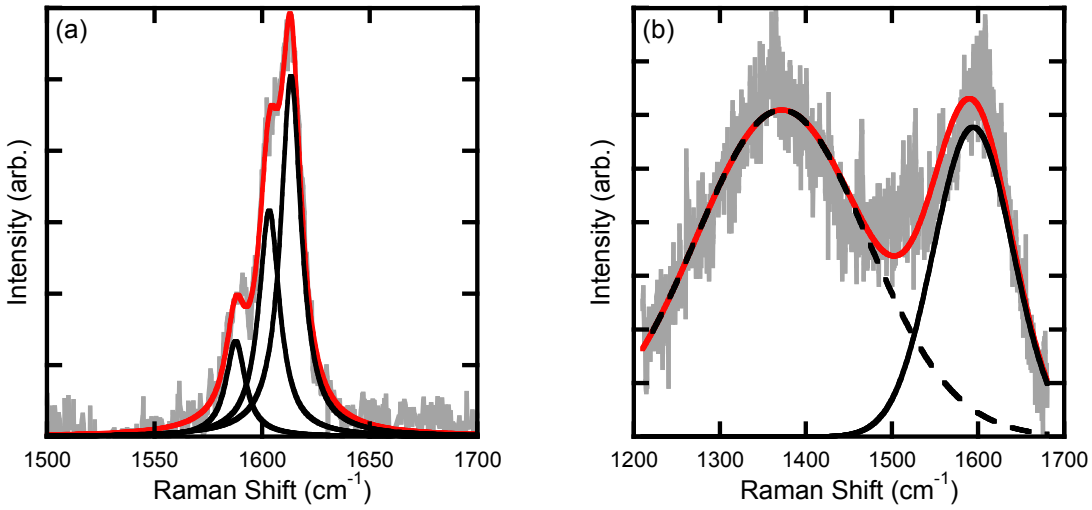

Figure 5.1 (a) The three components of the phenelyne peak for the Epon862 and Epikure 9553 composite matrix. (b) The D band (dotted) and G band of the carbon reinforcing fibers.

5.4 Results and discussion

For the first part of our investigation, we defined three types of epoxy containing regions within the composite and surveyed them using both Brillouin and Raman scattering. One region is the area between the braided layers of carbon. This region contains the largest volumes of epoxy that do not contain any fibers. The average thickness of this layer is around 300 μm. Because of the way we cut and polished our samples we can observe fibers in two orientations at the sample surface (Figure 5.2). The axial tows lay parallel to the sample surface so Brillouin scattering in the region between these fibers yields a modulus perpendicular to the fiber axis and tangential to its circumference. Finally, Brillouin measurements of the epoxy within the bias tows yield moduli in the direction 45° to the fiber axis. In addition to these three regions we also collected

Brillouin and Raman spectra from the bulk epoxy sample, and Raman spectra from lose carbon fibers.

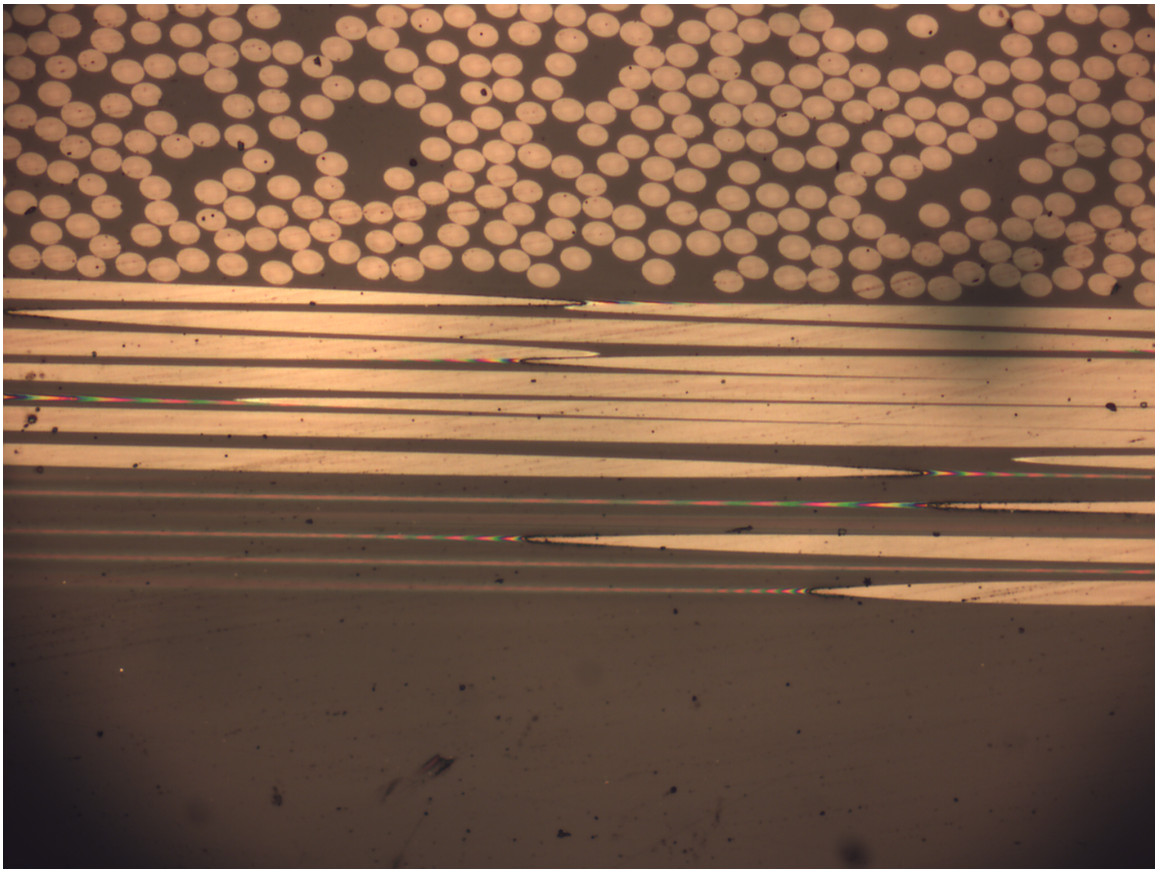

Figure 5.2 40X magnification light microscopy image showing the three types of regions that we analyzed: fibers 45° to the surface (top), parallel to the surface (middle), and epoxy regions between layers of fibers (bottom)

After analyzing the Brillouin spectra from this survey, we observe that both the epoxy between layers and the bulk epoxy have nearly the same average longitudinal modulus, 8.81 GPa and 8.77 GPa, respectively. Moreover the epoxy within a fiber tow, both measured at 90° and 45° to the fiber axis, shows a reduced longitudinal modulus (Figure 5.3). The modulus measured tangential to the fiber circumference and at 90° to the fiber axis averaged at 8.63 GPa. This corresponds to a 2.04% decrease in modulus as compared to the epoxy between

layers. When measured at 45° the average modulus was found to be 8.48 GPa, corresponding to a decrease of 3.75% from the between layer value.

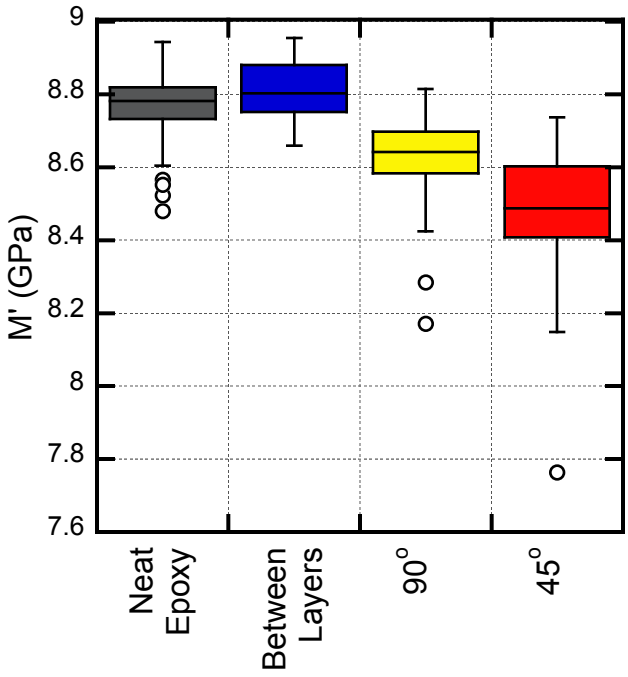

Figure 5.3 Box plot of the elastic moduli for three regions within the composite as compared to bulk epoxy

To determine the reason for this decrease, for example whether the observed differences in modulus result from residual stresses, we examine the positions of the three Raman peaks in the 1600 cm^{-1} region of the spectra obtained for the epoxy phase, which are attributed to phenylene rings, and compare them with the variation of the elastic moduli measured by Brillouin scattering. Straining the phenylene groups would cause the Raman peaks to shift, but we observe that the Raman peak positions remain essentially independent of the elastic modulus (Figure 5.4). Similarly, measurements of the D and G bands of the carbon fibers embedded in the composite do not reveal any conclusive information in terms of their state of strain, compared to that of

loose carbon fibers (Figure 5.5). The D and G bands of embedded fibers slightly shift compared to their positions in unconstrained fibers, but in opposite directions. If indeed bond straining caused such shifts, it would have to be in the same direction for both bands. These results suggest that the difference in modulus between bulk epoxy and epoxy contained within a fiber tow is not primarily related to residual stresses.

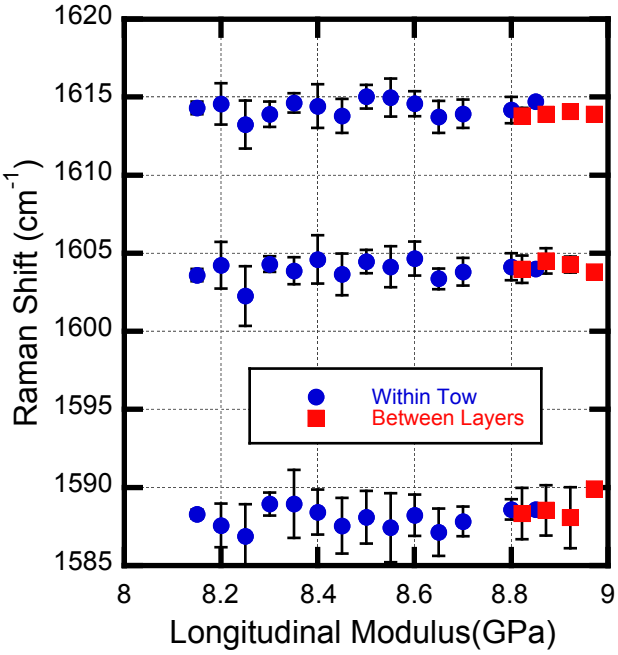

Figure 5.4 Raman Shifts vs M' for the three phenylene peaks of the epoxy matrix

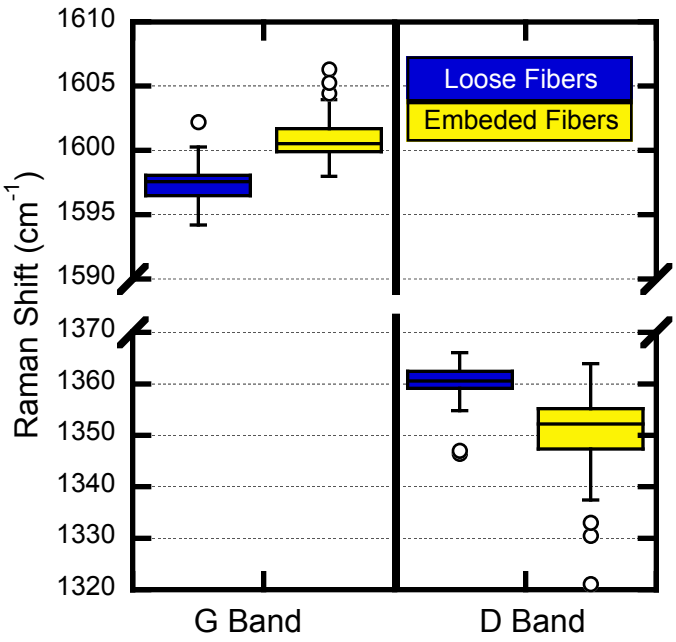

Figure 5.5 Raman shifts for the D and G bands of loose and embedded carbon fibers. No consistent shift is observed for which suggests that there is minimal difference in their states of stress.

The data in Figure 5.3 reveal the differences between the elastic responses of epoxy inside and outside of fiber tows, but do not correlate this response with the proximity to the fiber-epoxy interface. We therefore measured the longitudinal modulus of the epoxy as a function of the distance to the nearest interface. The results, summarized in Figure 5.6., reveal an apparent, albeit uncertainty-laden trend: the average value of the modulus decreases noticeably in close proximity of the fiber surface. However, the variance in the modulus increases significantly within about 5 μm of the interface. Inside a fiber tow, however, the distance to the surface of a given carbon fiber proves to be an incomplete metric. This measure fails to account for the influence fibers other than the one nearest to the laser spot. In a densely, yet somewhat irregularly

packed region of a tow, considering only the distance to the nearest fiber does not differentiate whether there is only one or several fibers close by the measurement location. Ultimately, we found the Gaussian-weighted local number density of fibers surrounding a given measurement point to yield the most consistent analysis. For this investigation, we chose to look only at the region containing fibers 45° to the sample surface, for which it is straightforward to count all fibers in the vicinity of a measurement point. We did not perform this analysis in regions where fibers are oriented parallel to the polished surface, as we cannot ascertain the arrangement of fibers beneath this surface.

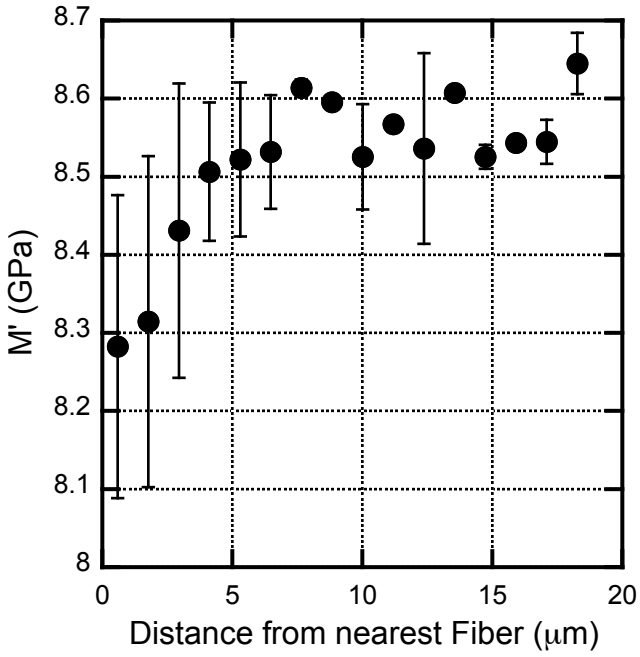

Figure 5.6 Longitudinal modulus as a function of the distance between the laser spot and the surface of the nearest carbon fiber

In this set of micro-Brillouin scattering experiments, we recorded the position of the laser spot and the locations of all visible fibers for each Brillouin spectrum we collected, allowing us to determine the distances from each position

of the Brillouin measurement to the centers of surrounding fibers. To calculate a local fiber density based on these distances, we must delineate the region of influence using a gradually decaying radial windowing function. A flat windowing function that truncates the region of influence at an arbitrary maximum distance can result in abrupt density fluctuations. Instead, we use a Gaussian windowing function, $e^{-r^2/2\sigma^2}/\left(2\pi\sigma^2\right)$, where *r* is the spatial coordinate, and σ is the standard deviation of the Gaussian. This windowing function smoothly decays with increasing distance from the point of measurement, weighing nearby fibers strongly while the effect of more distant ones fades rapidly. Accordingly, we calculate the local fiber density by integrating the windowing function multiplied with the Dirac delta function, $\delta\left(r-r_i\right)$, where r_i is the distance from the laser spot to the center of fiber *i*, and by summing over all fibers in the field of vision, i.e.,

$$\rho_F = \frac{1}{2\pi\sigma^2}\sum_i \int_0^\infty \delta(r-r_i)e^{\left(-r^2/2\sigma^2\right)}dr\,. \tag{5.2}$$

We can now relate the elastic modulus measured at a particular location with the local fiber density at that location. The result will depend to some extent on the choice of σ, which can be considered a measure of the extent of the region of influence. The data in Figure 5.6 already suggests that the observed effect of carbon fiber on the elastic properties of the epoxy matrix is localized roughly within 5 μm of the interface. Bracketing this value, we calculated ρ_F for each measurement point for a range of values of σ. For each value of σ, we calculated a linear regression of *M'* as a function of ρ_F. The inset of Figure 5.7 shows the correlation coefficient R^2 of the regressions as a function of σ. As σ is

increased, more fibers are accounted for by the windowing function, resulting in a sharp increase in correlation between *M'* and ρ_F. A maximum correlation is attained at σ = 3.9 μm. When σ is increased further, the correlation drops again and plateaus as σ approaches the size of our microscope's field of view. Accordingly, a window with a diameter of about 9.5 μm, assuming the full width at half maximum as a measure, most sensitively accounts for the effect the presence of fibers have on the final modulus of the epoxy matrix. A smaller window does not include all fibers that affect the elastic properties in their midst, and a larger window appears to encompass fibers that have no influence, i.e., the fluctuations in the local density arising from inhomogeneities in fiber packing needlessly causes scatter in the local density value. For σ = 3.9 μm 90% of the property changes have on average occurred within about 8.4 μm from the center of any given fiber, or 5.4 μm from its surface, which compares very well with the observed relationship between M' and the distance to the nearest fiber shown in fig 6. For this region, our data shows that the modulus decreases with increasing fiber number density as shown in Figure 5.7. The equation for the best fit line through the data is: $M' = 8.55 - 13.37\rho_F$. This data covers regions within a tow containing no fibers within the windowing function, to regions approaching the close packing limit, which for fibers 6 μm in diameter corresponds to a density of about 0.03 fibers/μm^2.

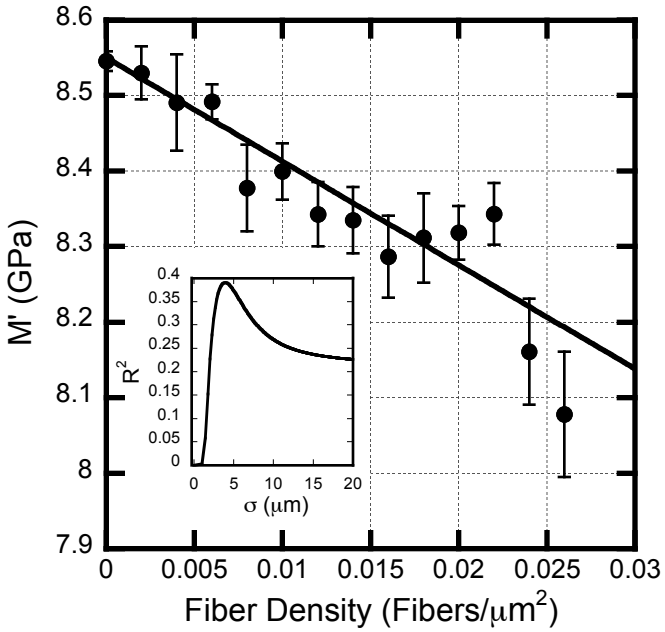

Figure 5.7 Longitudinal modulus vs fiber density (ρ_F) calculated with a σ = 3.9 μm. Inset: R^2 values for linear regressions of longitudinal modulus as a function of local fiber density for different values of σ.

5.5 Conclusions

Through our light scattering experiments we have demonstrated that the epoxy matrix within a fiber tow has a consistently lower elastic modulus than matrix epoxy found outside a tow. Furthermore we have determined that the modulus of the epoxy within a tow is correlated to the number density of nearby carbon fibers. The effect of fiber packing is most pronounced for regions of epoxy within 4.8 μm of a fiber's surface. Raman measurements suggest that the observed difference in modulus is not caused by stresses in the matrix. This leaves either chemical inhomogeneity of the epoxy, and/or structural reconfigurations of the epoxy network structure in the vicinity of the interface between fiber and polymer matrix as likely sources of the observed difference in

modulus. Future work with other matrix materials would shed more light on resolving these issues more definitively.

5.6 References

[1] Mijović J,Wang HT. Cure kinetics of neat and graphite-fiber-reinforced epoxy formulations. Journal of Applied Polymer Science 1989;37(9):2661-73.

[2] Possart W *et al.* Formation and structure of epoxy network interphases at the contact to native metal surfaces. Comptes rendus-Chimie 2006;9(1):60-79.

[3] Plepys AR,Farris RJ. Evolution of residual stresses in three-dimensionally constrained epoxy resins. Polymer 1990;31(10):1932-6.

[4] Corden TJ, Jones IA, Jones DT,Middleton V. The mechanisms of interlaminar cracking in thick resin transfer moulded composite cylinders. Composites Part A: Applied Science and Manufacturing 1998;29(4):455-64.

[5] Lincoln JE, Morgan RJ,Shin EE. Fundamental investigation of cure-induced microcracking in carbon fiber/bismaleimide cross-ply laminates. Polymer Composites 2001;22(3):397-419.

[6] Heinrich C, Aldridge M, Wineman AS, Kieffer J, Waas AM,Shahwan KW. Generation of heat and stress during the cure of polymers used in fiber composites. International Journal of Engineering Science 2012;53(85-111.

[7] Heinrich C, Aldridge M, Wineman AS, Kieffer J, Waas AM,Shahwan KW. The role of curing stresses in subsequent response, damage and failure of

textile polymer composites. Journal of the Mechanics and Physics of Solids 2013;61(5):1241-64.

[8] Song S, Waas AM, Shahwan KW, Xiao X,Faruque O. Braided textile composites under compressive loads: Modeling the response, strength and degradation. Composites Science and Technology 2007;67(15-16):3059-70.

[9] Brockenbrough JR, Suresh S,Wienecke HA. Deformation of metal-matrix composites with continuous fibers: geometrical effects of fiber distribution and shape. Acta Metallurgica et Materialia 1991;39(5):735-52.

[10] Rossoll A, Moser B,Mortensen A. Longitudinal deformation of fibre reinforced metals: influence of fibre distribution on stiffness and flow stress. Mechanics of Materials 2005;37(1):1-17.

[11] Heinrich C, Aldridge M, Wineman AS, Kieffer J, Waas AM,Shahwan K. The influence of the representative volume element (RVE) size on the homogenized response of cured fiber composites. Modelling Simul. Mater. Sci. Eng. 2012;20(7):075007.

[12] Llorca J *et al.* Multiscale Modeling of Composite Materials: a Roadmap Towards Virtual Testing. Advanced Materials 2011;23(44):5130-47.

[13] Sanctuary R, Bactavatchalou R, Muller U, Possart W, Alnot P,Kruger J, K. Acoustic profilometry within polymers as performed by Brillouin microscopy. Journal of Physics D: Applied Physics 2003;36(21):2738-42.

[14] Scarcelli G,Yun S. Confocal Brillouin microscopy for three-dimensional mechanical imaging. Nature Photonics 2007;2(39-43.

[15] Pastore C, Maria Giovanna, Parthenios J, Tsoukleri G, Cotugno S, Mensitieri G,Galiotis C. Assessing micromechanical behaviour of PET cords in rubber matrix composites by laser Raman microscopy. Composites Science and Technology 2013;85(0):104-10.

[16] Yeh WY,Young RJ. Molecular deformation processes in aromatic high modulus polymer fibres. Polymer 1999;40(4):857-70.

[17] Young RJ. Monitoring Deformation Processes in High-performance Fibres using Raman Spectroscopy. Journal of the Textile Institute 1995;86(2):360-81.

[18] Mock R, Hillebrands B,Sandercock R. Construction and performance of a Brillouin scattering set-up using a triple-pass tandem Fabry-Perot interferometer. Journal of Physics E: Scientific Instruments 1987;20(6):656-9.

[19] Kieffer J, Masnik JE, Nickolayev O,Bass JD. Structural developments in supercooled alkali tellurite melts. Physical Review B 1998;58(2):694-705.

[20] Wojdyr M. a general-purpose peak fitting program. Journal of Applied Crystallography 2010;43(5):1126-8.

[21] Sakata H, Dresselhaus G, Dresselhaus MS,Endo M. Effect of uniaxial stress on the Raman spectra of graphite fibers. Journal of Applied Physics 1988;63(8):2769.

Chapter 6

Conclusions and Future Work

The mechanical behavior of polymer matrix material in carbon fiber composites depends in part on the cure kinetics of the polymer, as well as the local arrangement of carbon fibers within the composite structure. By determining to what extent these attributes affect the mechanical properties of the matrix polymer, we can design new models that better represent the mechanical behavior of the composite material as a whole. Through the work presented in this thesis, we have developed a technique of concurrent Raman and Brillouin light scattering to concurrently measure the chemical and mechanical properties of a material. This technique was then applied to two curing polymer systems, DCPD and epoxy, to determine how their elastic properties evolve as a result of their curing processes. Concurrent Raman and Brillouin scattering was also applied to sectioned carbon fiber epoxy composite samples in order to measure the effect of the presence of carbon fibers on elastic properties of the epoxy matrix material. Together, these studies underline the effectiveness of combining Raman and Brillouin scattering to determine the relationship between chemistry and mechanical properties in evolving polymer systems. The results of both cure studies revealed an interesting mechanical equilibration behavior where the

mechanical modulus of the polymer continues to increase after the cure reaction has ended. Furthermore, the survey of sectioned carbon fiber samples revealed that the elastic modulus of the epoxy matrix depends on the packing density of the surrounding fibers.

DCPD polymerized with the aid of Grubbs catalyst was a good test case for using concurrent Raman and Brillouin scattering because the DCPD monomer is a fairly small organic molecule, with a limited number of Raman modes. More importantly, DCPD has a set of distinctive Raman modes associated with each of its reactive sites. Tracking the intensity of these peaks allows us to determine the degree of cure of the system and measure the contribution of each reactive site to the overall state of cure. Using this data, we constructed a kinetic model that describes the cure process as a function of the concentrations of reactive species in the system. The model suggests that the reaction rate of the DCPD depends on the square of the catalyst concentration, and that there is a minimum concentration below which the reaction will not progress. By combining the reaction information with the elastic modulus obtained by Brillouin scattering, we demonstrate that once the cure reaction has ended, the network continues to stiffen for some time. This phenomenon was modeled well by letting the species Φ_1 directly contribute to the modulus, and by attaching a time dependent term to the contribution to the modulus by the species Φ_2.

Using the same light scattering methods on curing a curing epoxy system yielded similar results to the DCPD. A lag in the development of the elastic

modulus was also observed when Epon 862 epoxy is cured with Epikure 9552 amine hardener. With the epoxy system, however, the lag in development of the elastic modulus appears to be dependent on the rate of reaction. This was tested by curing samples both at different temperatures and with different amine to epoxy ratios in order to change the reaction rate. We observe that for slow reactions, the relationship between modulus and cure is linear, while increasing the rate of reaction induces a deviation from linearity in this relationship. Modeling of the modulus to cure relationship suggests that, for a given degree of cure, there is an equilibrium value of the elastic modulus. When the system reacts quickly, changes in the network structure as a result of the cure reaction happen more quickly than the rate at which network equilibrates. For slow reaction conditions the network equilibrates at an equal with the cure reaction yielding a linear relationship between modulus and degree of cure. Heinrich et al. used an early version of this cure model to simulate the generation of heat and stress in a composite during cure.[1-3] In that model, the relationship between modulus and cure is considered to independent of reaction rate. By incorporating the rate dependent effects observed for the evolution of the elastic modulus, it should be possible to develop more accurate model of the stresses induced in the matrix during cure.

Finally, we surveyed sectioned and polished carbon fiber composite samples and measured the elastic modulus of regions between fiber tows as well as within them. This study confirmed that the inclusion of carbon fibers changes the elastic properties of the cured epoxy system. Our initial survey revealed that

the epoxy matrix between fiber tows has the same elastic modulus as bulk epoxy. However, epoxy within a tow, and therefore in close proximity to carbon fibers, has a modulus that is on average 3.75% lower than the bulk. Raman spectra of the same sample sites showed no correlation between the frequency shift of strain-sensitive peaks and the elastic modulus, suggesting that the observed difference in modulus is not due to residual stresses in the matrix. By analyzing images of the fibers around the location of each measurement, we determined that the packing density of the fibers in closest proximity to the measurement was well correlated to the observed elastic modulus. The effect of a given fiber only extends for about 5.4 μm from the fiber's surface. This result explains why the effect is only observed within a fiber tow, and not throughout all regions of the composite. The exact cause of the decreased modulus near the fiber surface remains undetermined, and could be related to such factors as: thermal gradients during cure, limited chemical diffusion and mixing between fibers, and chemical interactions between the epoxy and the fiber surface. Further experiments with other epoxy systems, other fiber compositions, and different processing conditions, may help determine the ultimate cause of this discrepancy in modulus.

These three studies have demonstrated the potential benefits of combining Raman and Brillouin light scattering methods. Together, they enable measurement of both mechanical properties and chemical structure in samples at both the bulk and micro scale. These techniques in combination with the carefully controlled chain growth and crosslinking reactions enabled by the

growing application of “click chemistry” may allow us to further probe the relationship between crosslinking and elastic modulus in polymer systems.[4] In the field of nano-composites, it may be possible to determine the mechanisms by which loads are transferred between polymers and reinforcing nanoparticles. Raman measurements of Pu/MTM clay films have shown that a strong Raman peak forms at 1150 cm-1 as strain is applied to the film.[5] This peak formation suggests a change in the structural configuration of the clay, the polymer or both. By straining samples and observing the changes in their Raman and Brillouin spectra, it may be possible to better understand how mechanical actuation can induce changes in both the chemistry and the mechanical properties of a material.

6.1 References

[1] Heinrich C, Aldridge M, Wineman AS, Kieffer J, Waas AM,Shahwan K. The influence of the representative volume element (RVE) size on the homogenized response of cured fiber composites. Modelling Simul. Mater. Sci. Eng. 2012;20(7):075007.

[2] Heinrich C, Aldridge M, Wineman AS, Kieffer J, Waas AM,Shahwan KW. Generation of heat and stress during the cure of polymers used in fiber composites. International Journal of Engineering Science 2012;53(85-111.

[3] Heinrich C, Aldridge M, Wineman AS, Kieffer J, Waas AM,Shahwan KW. The role of curing stresses in subsequent response, damage and failure of textile polymer composites. Journal of the Mechanics and Physics of Solids 2013;61(5):1241-64.

[4] Binder WH,Sachsenhofer R. Click Chemistry in Polymer and Materials Science. Macromol. Rapid Commun. 2007;28(1):15-54.

[5] L Sui, thesis, University of Michigan (2011).